Jin, Y.; Blawert, C.; Feyerabend, F.; Bohlen, J.; Silva Campos, M.; Gavras, S.; Wiese, B.; Mei, D.; Deng, M.; Yang, H.; Willumeit-Roemer, R.:
Time-sequential corrosion behaviour observation of micro-alloyed Mg-0.5Zn-0.2Ca alloy via a quasi-in situ approach.
In: Corrosion Science. Vol. 158 (2019) 108096.
First published online by Elsevier: 16.07.2019

https://dx.doi.org/10.1016/j.corsci.2019.108096

Time-sequential corrosion behaviour observation of micro-alloyed Mg-0.5Zn-0.2Ca alloy via a quasi-in situ approach

Yiming Jin[1]*, Carsten Blawert[2], Frank Feyerabend[1], Jan Bohlen[2], Maria Silva Campos[2], Sarkis Gavras[2], Björn Wiese[1], Di Mei[2], Min Deng[2], Hong Yang[2], Regine Willumeit-Römer[1,3]

1 Institute of Metallic Biomaterials, Helmholtz-Zentrum Geesthacht, 21502 Geesthacht, Germany

2 Magnesium Innovation Center, Helmholtz-Zentrum Geesthacht, 21502 Geesthacht, Germany

3 Faculty of Engineering, Christian-Albrechts-Universität zu Kiel, 24143 Kiel, Germany

*E-mail: yiming.jin@hzg.de

Abstract

The corrosion behaviour of as-cast and solution-annealed Mg-0.5Zn-0.2Ca alloy containing 150 ppm Si was investigated in 0.9% NaCl solution. The main secondary phases in the as-cast state are isolated MgCaSi and a coexisting intermetallic particle which consists of Mg_2Ca and $Ca_2Mg_6Zn_3$. A quasi-in situ approach is applied to investigate the corrosion initiation and development. It is proved that Mg_2Ca phase is anodic and preferentially corrodes within the first hour of immersion. Whereas, $Ca_2Mg_6Zn_3$ and MgCaSi phases continuously act as cathodes until 24 h. After solution annealing, the more homogeneous microstructure and reduced galvanic corrosion result in a higher corrosion resistance.

Keywords: A. Magnesium; A. Alloy; A. Intermetallics; B. SEM; B. TEM; C. Anodic dissolution

1. Introduction

Mg and many Mg alloys are promising candidates for biomedical applications [1-5]. The yield strength of pure Mg is lower than that of bones, and thus needs to be improved to meet the biomedical application demands [6]. Alloying proves to be an effective way to strengthen Mg. So far, a series of commercial alloys, e.g. AZ31, WE43, LAE442 [7, 8] and a number of independently developed alloys, e.g. Mg-Nd-Zn-Zr, Mg-Zn-Y-Nd [9, 10] have already been studied as potential candidates for biodegradable implant applications. However, most of them are Al- or rare earth-containing and the toxicity of the alloys still needs further investigations [11, 12].

Ca is an important element in human bones since it is beneficial for the bone regeneration [13]. However, although the addition of Ca could strengthen the mechanical properties, the corrosion rates of Mg-Ca alloys increase simultaneously with a higher content of Ca [14, 15]. It is well

known that the galvanic corrosion caused by potential difference between the intermetallic phases and the matrix is non-negligible in Mg alloys [16]. The optimal addition of Ca into the Mg matrix should be kept within 1 wt.% considering both the mechanical and corrosion properties [17]. Kim et al. [18] and Zeng et al. [19] claimed that galvanic corrosion of Mg-Ca alloys occurred with the Mg_2Ca phase as a cathode and the Mg matrix as an anode. Mohedano et al. [20] pointed out that the Mg_2Ca phase present a very small Volta potential difference compared to the Mg matrix (less than 10 mV), indicating inactive coupling on the Mg_2Ca/α-Mg interface. However, in recent years, a consensus in the literature has been reached that Mg_2Ca functions as the anode in the galvanic couple, which would be preferentially dissolved out of the matrices [13, 21-25]. Nonetheless, the conclusions were mostly drawn with the assistance of chromic acid to remove the corrosion products [13, 22, 24, 25]. Potentially, it is possible that chromic acid could remove Ca rich precipitates. In order to rule out this possibility, further investigations are needed without only using this potentially interfering reagent.

Mg-Zn alloys also attracted much attention since Zn is one of the essential elements in the human body and was found to be effective in strengthening Mg alloys [26]. The corrosion resistance of Mg alloys increased with the addition of Zn [27] and the suggested concentration in the Mg-Zn binary system should be kept below 5 wt.% [28]. It is reasonable to expect that with proper additions of Zn and Ca, a Mg-Zn-Ca ternary system with good corrosion and mechanical performance could be obtained. Du et al. [29] found that with the addition of Zn in a Mg-3Ca alloy, Mg-2Zn-3Ca exhibited improved mechanical strength, ductility and corrosion resistance. However, most of the previous studies focused on Mg-Zn-Ca alloys with a high addition of Ca [30] and/or Zn [24, 29, 31-34], which led to a high amount of intermetallic phases in the system. Song et al. [35] proposed that the continuous $Mg_{17}Al_{12}$ phase distributed along grain boundary could protect the Mg matrix from corrosion and Esmaily et al. [36] claimed that Al content is proportional to the corrosion resistance due to the formation of a protective Al-enriched layer in the surface film. However, unlike the Al-containing alloys, the continuous Mg_2Ca phase promoted pitting and undercutting of the Mg matrix [13, 29]. Bakhsheshi-Rad et al. [32] reported that the corrosion rate of Mg-0.5Ca-xZn alloys increased if the Zn content exceeded 1 wt.%. Zander et al. [37] pointed out that Mg-0.6Ca-0.8Zn possessed the lowest corrosion rate compared to other systems with higher Ca or Zn content. To balance the mechanical properties and the corrosion performance of Mg alloys, and to reduce potentially harmful effects of alloying elements, micro alloying is one method of choice. Although Mg-Zn-Ca alloys are emerging materials for biomedical applications, most of the

publications focused only on the general corrosion performance using electrochemical and physical methods [38-40]. Until now, few studies are committed to answer scientific questions: How does the corrosion initiate and develop? What is the corrosion sequence among the phases in the system? What are the causal links between macroscopic corrosion and microscopic corrosion? How to prove directly that Mg_2Ca is an anode without the use of reagent that might interfere with? To answer these questions, the alloy and experiments were designed and conducted.

In this study, the corrosion behaviour of a micro-alloyed Mg-0.5 wt.%Zn-0.2 wt.%Ca (hereafter, shortened as Mg-0.5Zn-0.2Ca) system was investigated. The intermetallics were discontinuous so that the corrosion interaction of a specific phase could be monitored and observed. Unlike many previous research on Mg alloys for biomedical applications, a simple 0.9 wt.% (shortened as 0.9%) NaCl solution rather than simulated body fluid (SBF) or Dulbecco's modified eagle medium (DMEM) was selected as the corrosive medium, so that more information from the material side could be obtained [41]. The general corrosion resistance of the as-cast and solution-annealed Mg-0.5Zn-0.2Ca alloy were compared and the corrosion mechanism was proposed based on a quasi-in situ monitoring method.

2. Experimental Procedures

2.1 Material preparation and compositional analysis

The as-cast Mg-0.5Zn-0.2Ca alloy was prepared by direct-chill casting with pure Mg (99.95 wt.%, Magnesium Elektron Ltd., UK), Zn (99.99 wt.%, Wilhelm Grillo Handelsgesellschaft mbH, Germany) and Ca (99.51 wt.%, Alfa Aesar GmbH & Co KG, Germany). The alloy melt was held at 720 °C under Ar-SF_6 protective atmosphere and then cast into steel moulds followed by water quenching. The steel moulds were coated with boron nitride and pre-heated up to 680 °C. The cast cylindrical ingots were 180 mm in length and 65 mm in diameter. To obtain a more homogeneous microstructure, solution annealing was applied. The ingots were annealed at 450 °C for 16 h followed by cold water quenching at room temperature. To verify the composition, Spark-Optical Emission Spectroscopy (Spark-OES, Spectrolab M9 Kleve, Germany) and Inductively Coupled Plasma-Optical Emission Spectroscopy measurements (ICP-OES, Thermo Fisher Scientific iCAP duo 6500, USA) were conducted.

According to the results from Spark-OES, the concentration of alloying elements and impurities in the top part and bottom part of the casting ingots are comparable, showing a homogeneous distribution of the alloying elements without sedimentation. Due to the similarity of Spark-OES and ICP-OES results, only the ICP-OES results are displayed in **Table 1**. The concentration errors for Zn and Ca are ± 0.02 wt.%. The deviations for the impurities are less than ± 6 ppm. Fe, Cu and Ni impurities which are well-known as detrimental to the corrosion properties are within the tolerance limits [42]. Interestingly, Si, which was sometimes not considered in the compositional analysis in previous investigations [24, 29, 39, 43] reaches almost 150 ppm. It might be derived from the raw materials during the casting process. Following an in depth literature review, it is found that limited research focused on the effect of Si addition on the corrosion performance of Mg alloys, possibly due to the comparatively low Volta potential difference between the Mg_2Si phase and Mg matrix [44, 45]. However, some other Si-containing phases might also form. The effect of minor Si inclusion on the microstructure and corrosion property of Mg-0.5Zn-0.2Ca alloy are elaborated in the following sections.

2.2 Microstructure analysis

The samples were wet ground with SiC abrasive paper up to 2500 grit consecutively and then polished with a mixture of water-free silica colloid (OPS) and 1 µm diamond slurry. To reveal the grain structure, the samples were treated by an acetic/picric acid etchant [46], followed by optical microscopy (OM, Leica DM2500 M, Germany) characterization. The grain size was calculated using a line intercept method [47] embedded in the software analySIS pro 5.0 (Olympus Soft Imaging Solutions GmbH, Germany) with multiple measurements. The microstructure was also characterized by scanning electron microscopy (SEM, Tescan Vega3, Czech Republic) and the compositions of intermetallic particles (IMPs) were determined by energy dispersive spectroscopy (EDS, IXRF Systems 550i, USA). Pandat software (CompuTherm LLC, USA) with the PanMagnesium 2017 database [48] was used to calculate the thermodynamic behaviour during the solidification process. The thermodynamic simulation was performed based on a Scheil model, which assumes that no diffusion takes place in the solid [49]. The overall area fraction of IMPs was calculated by using software ImageJ (National Institutes of Health NIH, USA) [50]. IMP analyses were performed by high energy X-ray diffraction (XRD) with a wave length of 0.01258 nm at PETRA III beamline in DESY and also by transmission electron microscopy (TEM, Philips CM200, Netherlands) with EDS detector (Oxford Instruments, UK). Twin-jet electropolishing using a 1.5% perchloric acid solution in

ethanol was used to prepare the TEM foils. Focused ion beam (FIB)/SEM dual beam microscope (FEI NOVA200, USA) was additionally used to prepare the TEM lamellae.

2.3 Electrochemical measurements

The general corrosion behaviour of the Mg-0.5Zn-0.2Ca alloy in 0.9 % NaCl solution was studied by potentiodynamic polarization (PDP) and electrochemical impedance spectroscopy (EIS) measurements using a potentiostat (Gill AC, ACM Instruments, UK). Prior to the test, all samples were ground until 1200 grit SiC abrasive paper. Connected to the potentiostat was a three-electrode cell set-up with Ag/AgCl as reference electrode, platinum mesh as counter electrode and the specimen as working electrode. The exposed sample area and the electrolyte volume were 0.5 cm^2 and 330 mL, respectively. During measurement, a magnetic stirrer at 200 rpm constantly agitated the electrolyte. The PDP tests were started at -150 mV relative to the free corrosion potential and performed at a scanning rate of 0.2 mV/s after being held at OCP for 30 min. The EIS measurements were carried out at OCP with an AC amplitude of ± 10 mV rms in the frequency range between 0.1 Hz and 30000 Hz. The EIS measurements were performed after different immersion times of 5 min, 1 h, 3 h, 6 h, 12 h, 24 h, 48 h and 72 h, respectively. All tests were repeated four times to guarantee the reliability of the results.

2.4 Quasi-in situ corrosion observation

All the samples were ground and polished following the aforementioned procedures. The samples were marked so that exactly the same position could be tracked before and after the corrosion process. A titanium tweezer was slightly applied on the sample surface to mark a small cross as a reference. Titanium tweezer rather than steel tweezer was chosen to guarantee that no iron residuals remained on the surface during the marking process. The distance between the targeted IMPs and the cross mark is 0.92 ± 0.07 mm. The IMPs and the surrounding matrix were observed with SEM in back scattered electron (BSE) and secondary electron (SE) mode. Prior to the corrosion test, the sample was carefully polished again to further reduce the effects of marking and electron exposure on the corrosion performance. After immersion in 0.9% NaCl solution for a specific time, i.e. 0.5 min, 10 min, 30 min, 1 h, 3 h, 6 h, 12 h or 24 h, respectively, the corroded samples were rinsed with deionized water and ethanol to remove the crystallized NaCl and poorly attached corrosion products. Then, the same positions were observed again by SEM in BSE and SE mode directly after immersion as well as after the removal of the corrosion products. Diluted chromic acid (~1.5 g/L) cleaning and a mechanical exfoliation process (repeated peeling with sticky tape) were applied to study the corrosion process development.

3. Results and Discussion

3.1 Microstructural analysis

Microstructures of the as-cast and solution-annealed Mg-0.5Zn-0.2Ca alloys were characterized by OM and SEM. The as-cast Mg-0.5Zn-0.2Ca alloy revealed a dendritic microstructure with IMPs present along the grain boundary and within the grains (**Fig. 1a, b**). Zn is enriched in the interdendritic arms and grain boundaries which are pointed with arrows in Fig. 1b. For clearer interpretation, EDS element mapping results of the as-cast state are also shown in supporting information (**Fig. S1**). The average grain size was 147 ± 8 μm. By analysing the morphologies and compositions of numerous precipitates via SEM and EDS, three types of secondary phases are identified to be present in the alloys (**Fig. 1c, d**). IMPs are formed due to the low solid solubility of Si in Mg matrix (maximum 0.003 at.%) [5, 51]. The Mg-Ca-Si-containing phases had either spherical or elongated shape. They are distributed within grains and along grain boundaries. Coexisting intermetallic particles (CE-IMPs) with composition and morphology contrast can also be observed. The brighter part is Mg-Zn-Ca-containing phase and the darker part is Mg-Ca-containing phase. The CE-IMPs are either round or elongated and located within grains. In addition, a limited amount of isolated Mg-Zn-Ca-containing particles can also be observed. Although the shape and brightness of the isolated Mg-Zn-Ca- and Mg-Ca-Si-containing particles are similar in BSE image, clear discrepancy in SE image can still be seen. Nevertheless, it is not the focus of this work due to its rare in quantity.

The SEM EDS semi-quantitative measurement results of the IMPs in the as-cast state are listed in **Table 2**. The relative atomic ratio of Ca/Si in the Mg-Ca-Si-containing phase is 0.81 ± 0.09. As reported by Carbonneau et al. [52], the atomic fraction among Mg, Ca and Si was close to a stoichiometric value of one-third in the ternary MgCaSi phase. In this case, the atomic ratio of Ca/Si is near 1, indicating that the Mg-Ca-Si-containing phase is potentially a MgCaSi phase. The atomic ratio of Zn/Ca in Mg-Zn-Ca part in CE-IMP is 1.59 ± 0.41, which indicates that the Mg-Zn-Ca part in CE-IMP is possibly $Ca_2Mg_6Zn_3$ [33]. The average Zn concentration in Mg-Ca part in CE-IMP is approximately 3 at.%, which is probably from the Mg-Zn-Ca part in the neighbourhood. Since only one IMP forms between Mg and Ca, it could be assumed that the Mg-Ca part in CE-IMP is the Mg_2Ca phase. The overall IMPs area fraction in the as-cast state is calculated to be 0.29 ± 0.05% by ImageJ. However, it is hard to measure the fraction of every single phase since the size of the IMP is just several microns. Considering the main

phases in the system, the quantity fraction of CE-IMP and MgCaSi are measured and the values are 45.6 ± 4.8% and 54.5 ± 4.8%, respectively.

To confirm the crystal structures of IMPs, high energy XRD in DESY was conducted. Other than the well-established α-Mg peaks, no obvious peaks in the spectrum are detected (not shown here). This is probably due to the fact that the amount of IMPs in this micro-alloyed system is below the detection limit of the XRD measurement [53, 54]. In addition, selected area electron diffraction (SAED) analysis of MgCaSi and CE-IMP were also conducted in TEM. Both phases in CE-IMP possess a hcp crystal structure with two distinct lattice spacing. The hcp phase with a larger lattice spacing in reciprocal space (**Fig. 2a**) corresponds to Mg_2Ca phase and the hcp phase with a smaller lattice spacing in reciprocal space (**Fig. 2b**) corresponds to $Ca_2Mg_6Zn_3$ phase. These results are in accordance with the literature, which stated that Mg_2Ca phase possessed smaller lattice parameters while $Ca_2Mg_6Zn_3$ phase had larger lattice parameters [55, 56]. MgCaSi phase possesses a primitive orthorhombic crystal structure (**Fig. 2c**) [52]. All these SAED patterns confirmed prior research performed for these phases [54, 57-62]. TEM EDS spot analyses (**Fig. 2d**) on Mg_2Ca part (x1) and $Ca_2Mg_6Zn_3$ part (x2) in CE-IMP, and MgCaSi (x3) are consistent with the validated SEM EDS results **(Fig. 1d)**. Cu signal is detected from the TEM sample holder.

According to the solidification simulation by Pandat^{TM}2017 (database PanMagnesium 2017) [48] using a Scheil model [49] (**Fig. 3**), α-Mg starts to form at 647.26 °C followed by the precipitation of MgCaSi at 634.89 °C. This suggests that MgCaSi phase solidifies at an early stage between the dendrite arms while α-Mg grains are forming. The precipitation of $Ca_2Mg_6Zn_3$ begins at 393.88 °C and the last drop of liquid exhausts at 393.82 °C. With further cooling at 393.80 °C, Mg_2Ca starts to precipitate. Due to the similar solidification temperatures of $Ca_2Mg_6Zn_3$ and Mg_2Ca phases (less than 0.1 °C difference), it can be inferred that they solidify almost simultaneously and $Ca_2Mg_6Zn_3$ acts as a nucleation site when Mg_2Ca starts to precipitate. This is in accordance with the present distribution in as-cast state that $Ca_2Mg_6Zn_3$ embraces Mg_2Ca in CE-IMP (**Fig. 1c**).

After solution annealing at 450 °C for 16 h, the microstructure becomes more homogeneous, the average grain size slightly increases to 164 ± 3 μm and no segregation of Zn can be detected (**Fig. 4a, b**). The solution annealing parameters are chosen based on the thermodynamic calculated phase diagrams of Mg0.5Zn-Ca (**Fig. S2**) and Mg0.5Zn0.2Ca-Si systems (**Fig. S3**)

and some previous works [63-67]. Considering the inclusion of Si, it is predicted by Pandat [48] that the MgCaSi phase cannot be dissolved under the selected annealing condition. In addition, based on the EDS results (**Table 2**), the $Ca_2Mg_6Zn_3$ phase and the Mg_2Ca phase from CE-IMP cannot be recognized after the solution annealing, which is consistent with previous findings [33] and thermodynamic calculation. Zn from the $Ca_2Mg_6Zn_3$ phase dissolves into the Mg matrix and Ca from the $Ca_2Mg_6Zn_3$ or the Mg_2Ca phase either dissolves into the matrix or is attracted to the surrounding MgCaSi phase. MgCaSi possesses a low diffusion efficiency in the Mg matrix [52] and therefore prevails as the dominant secondary phase in the solution-annealed Mg-0.5Zn-0.2Ca alloy with an area fraction of 0.15 ± 0.02% (**Fig. 4c, d**).

3.2 Electrochemical measurements

PDP and EIS were employed to characterize and compare the general corrosion performance of the as-cast and solution-annealed alloy. According to the PDP curves, the corrosion potential moves towards the positive direction after solution annealing (**Fig. 5**). The pitting potential of the polarization curve shows the likelihood of localized corrosion, and a more positive value implies a less likely localized corrosion [29, 68]. It is visible from the polarization curves that the pitting potential of the solution annealed sample is more positive than that of the as-cast sample, revealing a more compact or protective layer on the surface after solution annealing.

EIS was measured for 72 h over a frequency range from 30000 Hz to 0.1 Hz, considering that lower frequencies (such as ~0.01 Hz) would induce a pseudo-inductive loop [69, 70]. In order to see the curves more clearly and also not to sacrifice the overall trend, only the results after 5 min, 1 h, 6 h, 12 h, 24 h and 72 h immersion are presented here. For as-cast Mg-0.5Zn-0.2Ca alloy, two time constants are observed during the first 6 h immersion, as indicated by the Nyquist plot (**Fig. 6a**). The first time constant within high-to-medium frequency region (around 100 Hz) is related to the resistance of the oxide film on the surface. The second time constant at low frequency (1 Hz to 0.1 Hz) is associated with the charge transfer process at double layer [71]. After 12 h and 24 h, only one capacitive loop is observed with some scattered points in the low frequency range, indicating active mass transport that happens on the sample surface. With further immersion, two time constants can be seen again. In contrast, two time constants are present during the entire immersion period for the solution annealed state (**Fig. 6b**).

The increase in the depressed semicircle diameter is related to a better corrosion resistance. The total resistance (R_t) at 0.1 Hz is the sum of oxide layer resistance and charge transfer

resistance, and the R_t values of the as-cast and solution-annealed samples during immersion are shown in **Fig. 6c**. For as-cast Mg-0.5Zn-0.2Ca, the R_t value at 0.1 Hz increases steadily from 670 $\Omega \cdot cm^2$ to 1320 $\Omega \cdot cm^2$ upon immersion until 6 h, demonstrating the densification and thickening of the semi-protective corrosion product layer. After that, the R_t value drops sharply at 12 h, implying that the alloy suffers from localized corrosion attack. It is well known that Cl^- ion presence is detrimental to the alloy's corrosion performance considering its penetration and pitting promoting effect [72]. With prolonged exposure until 72 h, an increase in the R_t value can be observed again, which is possibly due to the precipitation of corrosion products dominates over the dissolution of the alloy. During this comparatively longer time interval (1 measurement per day), the samples are covered with thicker and more protective corrosion product layers. For solution-annealed sample, the R_t value increases steadily until 12-24 h and suffers a little loss afterwards. The dramatic loss of R_t value occurs in the as-cast state is not observed in the solution annealed counterpart. Although there is a slight decline after 24 h possibly due to localized corrosion, the respective time of occurrence is also delayed. By comparing the R_t values of the two states, the solution-annealed one exhibits a better corrosion resistance during the whole immersion process, which might be due to the following reasons: The lower amount of IMPs after solution annealing leading to a less pronounced galvanic corrosion between the matrix and the IMPs. Furthermore, with the dissolution of Zn segregations at the grain boundaries and Zn-containing precipitates, the homogeneous microstructure of solution-annealed state results in a more uniform corrosion behaviour.

The consistent results from PDP and EIS give evidences that the corrosion resistance of the solution-annealed sample is higher.

3.3 Quasi-in situ corrosion observation

The quasi-in situ immersion test is a useful method to investigate the initiation of corrosion on a microscopic scale [69, 73]. To explain the general corrosion performance described in section 3.2 and to elucidate the corrosion mechanisms of Mg-0.5Zn-0.2Ca alloy, this approach was adopted.

Reviewing literature, chromic acid was used by most of the researchers to remove the corrosion products, and they claimed that only negligible effect was caused to the alloys [43, 74]. However, it cannot be applied to the Mg-Zn-Ca system. It appeared that the IMPs and the matrix in the as-cast sample are heavily etched when exposed to fresh chromic acid (180 g/L)

for 5 min (**Fig. 7a, b**). In addition, the Mg_2Ca phase in CE-IMP is found to interact with even 100 times diluted chromic acid (~ 1.5 g/L) while $Ca_2Mg_6Zn_3$ and MgCaSi phases remain (**Fig. 7c, d**). To exclude the effect of chromic acid on the corrosion morphology, a new methodology needs to be developed.

Inspired by Novoselov and Geim [75], scotch tape was applied to peel off the corrosion products to elucidate the corrosion process. After only 30 s exposure to 0.9% NaCl solution, there are already discernible thin corrosion products forming on both the matrix and the IMPs (**Fig. 8a, d, g**). With prolonged exposure for 10 min and 30 min, the corrosion products become thicker but the inherent contrast in CE-IMP can still be observed **(Fig. 8b, e, h**), which demonstrates that the IMPs are at least not fully corroded. CE-IMPs are entirely covered with the corrosion products that blur the phase contrast subsequent to 1 h immersion (**Fig. 8c, f**). After being peeled off by scotch tape, it is discovered that the greyish part which used to be the Mg_2Ca phase is no longer present, whereas the brighter part which used to be $Ca_2Mg_6Zn_3$ phase still remains (**Fig. 8i and Fig. S4**). According to the EDS spot analysis (**Fig. 8j**), trace amount of Ca can be detected in Point 1, which hints that the Mg_2Ca phase is dissolved. The slight Zn and Ca signals are possibly from the $Ca_2Mg_6Zn_3$ in the vicinity or from the Mg_2Ca phase residuals underneath. In contrast, evident Zn and Ca signals are captured in Point 2. The post-processing of the immersion test are water and acid free. This result can be a direct evidence that the corrosion is inclined to happen first in the CE-IMP area, and out of which, the Mg_2Ca phase is preferentially dissolved within 1 h immersion leaving $Ca_2Mg_6Zn_3$ phase uncorroded.

The similar corrosion morphology observed after diluted chromic acid cleaning and tape-peeling are shown in **Fig. S5**. Considering the facts that $Ca_2Mg_6Zn_3$ and MgCaSi phases are not affected by diluted chromic acid cleaning and Mg_2Ca is already dissolved after 1 h, the corrosion products are thoroughly removed with it afterwards. CE-IMPs are completely covered and MgCaSi are partially covered with the corrosion products subject to 1 h immersion (**Fig. 9f**), implying that the corrosion kinetics of Mg/CE-IMP interface is stronger than that of the Mg/MgCaSi interface. After cleaning, the corrosion products and Mg_2Ca phase are removed whereas $Ca_2Mg_6Zn_3$ and MgCaSi phases remain (**Fig. 9k**). Various galvanic couples exist in the as-cast sample. Within CE-IMP, Mg_2Ca dissolves preferentially following **Eq. 1** and $Ca_2Mg_6Zn_3$ phase acts as the cathode following **Eq. 2** [76]:

$$Mg_2Ca_{(s)} \rightarrow 2Mg^{2+} + Ca^{2+} + 6e^- \quad (1)$$

$$H_2O + 2e^- \rightarrow H_2 + 2OH^- \quad (2)$$

In addition, CE-IMP acts as the cathode in overall following **Eq. 2**, and its surrounding Mg matrix functions as the anode according to **Eq. 3** [76]:

$$Mg \rightarrow Mg^{2+} + 2e^- \quad (3)$$

This is in good agreement with the claims of Du et al. [29] on the order of the Volta potential: $0 > Ca_2Mg_6Zn_3 > Mg > Mg_2Ca$. The phase in negative direction of the Volta potential series is more inclined to be corroded which functions as the anode in the galvanic couple. Moreover, the MgCaSi phase with a positive Volta potential difference relative to the Mg matrix also serves as effective site for localized corrosion initiation [26, 45]. The cathodic $Ca_2Mg_6Zn_3$ and MgCaSi phases remain after 1 h immersion and cleaning process, revealing that the galvanic corrosion derive from $Ca_2Mg_6Zn_3$/Mg and MgCaSi/Mg couples will continue. After 3 h, the Mg matrix near CE-IMP starts to be undermined while the matrix in the vicinity of the isolated $Ca_2Mg_6Zn_3$ or MgCaSi shows comparatively less corrosion (**Fig. 9g, l**). This might be due to the larger Volta potential difference of $Mg_2Ca/Ca_2Mg_6Zn_3$ and Mg/CE-IMP than $Mg/Ca_2Mg_6Zn_3$ and Mg/MgCaSi, which drive more intense oxidation-reduction reactions at the respective interface. The undermined Mg matrix area is even larger after 6 h. Galvanic corrosion would terminate only if the $Ca_2Mg_6Zn_3$ phase in position II were detached (**Fig. 9c, h, m**). With 12 h and 24 h exposure, cracks are found in the much thicker corrosion layers due to the dehydrating process. Although the pit depth and surface roughness increase, the majority of $Ca_2Mg_6Zn_3$ and MgCaSi phases are still present on the surface (**Fig. 9n, o**), indicating the continuous galvanic corrosion at the specific interface.

The same procedure was also applied to the solution-annealed sample with only Mg/MgCaSi galvanic couple present in the system. With 1 h exposure, only moderate corrosion attack occurs at the interface (**Fig. 10k**). The Mg matrix surrounding MgCaSi phase corrodes according to **Eq. 3**. After 3 h, MgCaSi is fully covered with the corrosion products (**Fig. 10l**) and some places start to be undermined subject to 6 h immersion (**Fig. 10m**). After 12 h and longer exposure durations, the corrosion products become thicker (**Fig. 10i, j**). Cracks are formed along the IMPs possibly due to the active interaction at the interface. The degradation of matrix is more severe with increasing the immersion time (**Fig. 10n, o**).

Comparing the corrosion morphology of the two states on a larger scale, it seems that the corrosion near the grain boundary in the as-cast sample (**Fig. 11a**) is more pronounced than that in the solution-annealed sample (**Fig. 11b**). Due to the segregation of Zn, the Volta potential at the grain boundary area is more positive than that of the inner grain area, thus causing galvanic corrosion at the grain boundary interface. In contrast, Zn is uniformly distributed in the solution-annealed sample and corrosion develops homogeneously. Moreover, selective corrosion occurs at the edge of the as-cast sample after 6 h possibly due to the crystallographic orientation [77] (**Fig. 11c**), and it propagates towards the interior of the sample extensively afterwards. However, the selective corrosion is not observed during the entire immersion process for solution-annealed sample due to its more homogeneous microstructure.

3.4 Links between micro and macro scale corrosion

For as-cast sample (**Fig. 12a**), the intense galvanic corrosion between $Ca_2Mg_6Zn_3$ and Mg_2Ca in CE-IMP weakens due to the consumption of the Mg_2Ca phase after 1 h immersion (**Fig. 9a, f, k**). Although the continuously presenting of Mg/$Ca_2Mg_6Zn_3$ and Mg/MgCaSi galvanic couples during immersion, the corrosion layer is built up upon immersion within the first 6 h as indicated by the quasi-in situ observation (**Fig. 9 f, g, h**). These correspond with the steady increase of R_t value at 0.1 Hz (**Fig. 6c**) and the increasing semicircle at the middle frequency (**Fig. 6a**) from the EIS results. After 12 h, the galvanic corrosion of Mg/$Ca_2Mg_6Zn_3$ and Mg/MgCaSi proceed and the matrix selective corrosion develops into a larger scale, which destroy the integrity of the corrosion film. Cl^- ions can penetrate through the loose corrosion layers and react with the Mg matrix underneath. This is in accordance with the dramatic decrease of R_t value in the EIS measurement at 12 h. For solution annealed sample (**Fig. 12b**), less amount of galvanic couple (only Mg/MgCaSi) contributes to less pronounced corrosion. In addition, the homogeneous microstructure formed during solution annealing contributes to uniform corrosion. All these lead to a higher R_t value for solution-annealed sample at each time.

3.5 Summary and outlook

Although some previous research also used NaCl solution to characterize the corrosion behaviour of biodegradable Mg alloys [71, 78-80], various simulated physiological fluids were used to mimic the corrosive atmosphere in biological body, such as Kokubo's SBF [81], revised SBF [82], Hank's solution [83], cell culture medium (like DMEM) [84], phosphate buffer solution (PBS) [85] and 0.9% NaCl solution. The corrosion performance of Mg alloys differ greatly in these media. Considering the ultimate target for biomedical applications, the usage

of media with compositions closer to the body fluids seems to make more sense than the simple NaCl solution. Nevertheless, the authors choose 0.9% NaCl solution due to the following considerations:

1. NaCl solution is the only medium that is used by researchers for both structural and biomedical applications. The present study is dedicated to provide information to the existing database that is in association with the studies of corrosion scientists, degradation scientists and metallurgists.

2. It was suggested that the synergistic effect of Ca^{2+}, Mg^{2+}, HPO_4^{2-} and HCO_3^- in solution promoted the formation of a protective layer on Mg alloy surface [73]. The corrosion progress might be suppressed due to the precipitation of inorganic products on the IMPs. In contrast, NaCl solution is much simpler and the formed corrosion products ($MgO/Mg(OH)_2$) in NaCl are not protective, so that more information from the material side could be obtained, especially during the early stage of immersion. Through the published work, like Ref. [73], it could be found that the co-precipitation Ca-P-C corrosion products are preferentially formed around iron impurities which are the starting points of galvanic corrosion. Thus, with the results obtained in NaCl solution, the corrosion initiation and corrosion sequence of the intermetallics as well as the corrosion products formation process in SBF-like media are possible to be cautiously predicted.

3. As this is an ongoing research, the interaction of Mg-Zn-Ca alloy and more sophisticated media will also be studied so that the results can be compared.

In order to avoid the effect of chromic acid, a repeated peeling process was introduced to remove the corrosion products after immersion. It is a good way to reveal the corrosion sequence of IMPs in the alloys without the interference of water and/or acid, especially for the Mg-Zn-Ca system. However, this non-destructive exfoliation technique is not efficient in removing the corrosion layers. When it comes to the sample that immersed in SBFs or cell culture medium, the efficiency of this peeling method might be even lower considering the thicker/more protective/more firmly-adherent layer on top. The feasibility of which on Mg alloys immersed in these media remains an open question.

Zhang et al. [86] used scanning transmission electron microscopy (STEM) equipped with EDS and Matsubara et al. [87] used electron probe microanalysis (EPMA) to quasi-in situ observe the corrosion development of Mg alloys. Repeated interrupted immersion of the same sample was adopted to reflect its corrosion progress. However, during this process, the corrosion

products might change due to the reaction between $Mg(OH)_2$ and CO_2 in the atmosphere [88, 89], which might be divergent from the case in continuous immersion. This influence was avoided in our study by using different samples with continuous immersion duration. In addition, the effect of electron exposure during microscopy on the sample surface condition is reduced by further polishing before the immersion test, so that the fresh sample surface is exposed.

Precisely speaking, the results here are only applicable to the materials with the same composition, preparation methods, processing routes and experimental conditions. But potentially, they are also transferrable to the Mg-Zn-Ca system with different composition due to the formation of similar IMPs. In a broader sense, some part of the conclusions may be appropriate for other Mg alloys. For example, chromic acid was found to etch Mg_2Ca phase in this study, which may be also applicable to other anodic IMPs such as the secondary phase in cast EW75 alloy [90] due to the acceleration reaction in acidic atmosphere. The diluted chromic acid cleaning together with repeated tape-peeling might be an option for the corrosion products removal of alloys containing anodic IMPs. Si was found to form MgCaSi phase in this study which might be applicable to the formation of other Si containing precipitates in other Mg alloys. In addition, small FeSi-containing impurity particles were found in pure Mg which affect the corrosion performance heavily [91, 92]. The Si concentration should be thoroughly measured and carefully controlled for all Mg alloys. For future research, special attention has to be paid to the impurities in traditional sense, e.g. Fe, Cu, Ni, as well as other elements that can form stable IMPs in the system, e.g. Si. Although the as-wrought alloys possess better corrosion and mechanical properties compared to the as-cast counterpart [15, 93], it is easy to anticipate that the tracking of the small IMPs in as-wrought state is even harder. However, the corrosion sequence information indicated in this study might be pertinent to the one in as-wrought state due to the unchanged nature of the IMPs.

4. Conclusions

In this study, microstructure and the corrosion performance of as-cast and solution-annealed Mg-0.5Zn-0.2Ca were investigated and compared. Three IMPs were recognized in the as-cast state using SEM and TEM: $Ca_2Mg_6Zn_3$ and Mg_2Ca in CE-IMP and isolated MgCaSi. The general corrosion performance was characterized by electrochemical methods. The corrosion sequence of the IMPs and the corrosion mechanism were unveiled via quasi-in situ corrosion observation. The conclusions are drawn as follows:

(1) Corrosion occurs once the alloy is immersed in the medium. Mg_2Ca in CE-IMP is experimentally shown to be the most anodic phase respective to other IMPs and the matrix. It will corrode preferentially within the first hour of immersion in 0.9% NaCl solution, whereas $Ca_2Mg_6Zn_3$ and MgCaSi are effective cathodes which remain even after 24 h immersion. The nature of IMPs and their corresponding corrosion time are not only beneficial for understanding the corrosion mechanism, but also helpful for the design and development of new lifetime-scalable implant material.

(2) It is observed that 150 ppm Si already causes formation of MgCaSi in Mg-Zn-Ca alloy. The amount of MgCaSi are as many as the number of particles produced by the main alloying elements (CE-IMP), suggesting that the tolerance limit of Si in Mg-Zn-Ca alloy should be far less than 150 ppm. The MgCaSi phase is relatively stable, which will remain after solution annealing and continuously function as a cathode.

(3) Chromic acid should be utilized cautiously to remove the corrosion products of Mg alloys. It is found that fresh chromic acid etches the as-cast Mg-Zn-Ca alloy and the diluted one still dissolves Mg_2Ca phase. In this work, diluted chromic acid cleaning combined with a mechanical exfoliation process were used for surface cleaning after corrosion testing. However, new methods are still demanded, which should be harm-free and efficient.

(4) After the solution annealing, the corrosion resistance increases due to the reduced galvanic couples. Selective corrosion is not observed due to the more homogeneous microstructure. It is possible to tailor the corrosion behaviour by adjusting the microstructure via heat treatment. The microscopic corrosion observation matches well with the macroscopic corrosion performance.

Acknowledgments

Yiming Jin thanks China Scholarship Council for the award of fellowship and funding (201604910527). The authors thank Mr. Günter Meister, Mr. Gert Wiese, Dr. Domonkos Tolnai, Dr. Yuanding Huang, Dr. Henry Ovri, Mr. Xiao Zhang and Mr. Ulrich Burmester from HZG for the help of sample preparation and characterization. Mr. Eshwara Nidadavolu is thanked for Spark-OES measurement and manuscript revision. Ms. Katharina Strecker, Ms. Julia Bode and Prof. Carla Vogt from Technische Universität Bergakademie Freiberg are greatly acknowledged for ICP-OES measurement.

Declarations of interest

The authors declare that there is no confliction of interest.

Data availability

The raw/processed data required to reproduce these findings cannot be shared at this time as the data also forms part of an ongoing study.

References

[1] F. Witte, The history of biodegradable magnesium implants: A review, Acta Biomaterialia, 6 (2010) 1680-1692.
[2] G. Song, A. Atrens, Understanding Magnesium Corrosion—A Framework for Improved Alloy Performance, Advanced Engineering Materials, 5 (2003) 837-858.
[3] M.T. Andani, N. Shayesteh Moghaddam, C. Haberland, D. Dean, M.J. Miller, M. Elahinia, Metals for bone implants. Part 1. Powder metallurgy and implant rendering, Acta Biomaterialia, 10 (2014) 4058-4070.
[4] M.P. Staiger, A.M. Pietak, J. Huadmai, G. Dias, Magnesium and its alloys as orthopedic biomaterials: A review, Biomaterials, 27 (2006) 1728-1734.
[5] M. Esmaily, J.E. Svensson, S. Fajardo, N. Birbilis, G.S. Frankel, S. Virtanen, R. Arrabal, S. Thomas, L.G. Johansson, Fundamentals and advances in magnesium alloy corrosion, Progress in Materials Science, 89 (2017) 92-193.
[6] G. Song, Control of biodegradation of biocompatable magnesium alloys, Corrosion Science, 49 (2007) 1696-1701.
[7] E. Willbold, A.A. Kaya, R.A. Kaya, F. Beckmann, F. Witte, Corrosion of magnesium alloy AZ31 screws is dependent on the implantation site, Materials Science and Engineering: B, 176 (2011) 1835-1840.
[8] F. Witte, V. Kaese, H. Haferkamp, E. Switzer, A. Meyer-Lindenberg, C.J. Wirth, H. Windhagen, In vivo corrosion of four magnesium alloys and the associated bone response, Biomaterials, 26 (2005) 3557-3563.
[9] J. Liu, B. Zheng, P. Wang, X. Wang, B. Zhang, Q. Shi, T. Xi, M. Chen, S. Guan, Enhanced in Vitro and in Vivo Performance of Mg–Zn–Y–Nd Alloy Achieved with APTES Pretreatment for Drug-Eluting Vascular Stent Application, ACS Applied Materials & Interfaces, 8 (2016) 17842-17858.
[10] X. Zhang, G. Yuan, L. Mao, J. Niu, W. Ding, Biocorrosion properties of as-extruded Mg–Nd–Zn–Zr alloy compared with commercial AZ31 and WE43 alloys, Materials Letters, 66 (2012) 209-211.
[11] F. Feyerabend, J. Fischer, J. Holtz, F. Witte, R. Willumeit, H. Drücker, C. Vogt, N. Hort, Evaluation of short-term effects of rare earth and other elements used in magnesium alloys on primary cells and cell lines, Acta Biomaterialia, 6 (2010) 1834-1842.
[12] J. Chen, L. Tan, X. Yu, I.P. Etim, M. Ibrahim, K. Yang, Mechanical properties of magnesium alloys for medical application: A review, Journal of the Mechanical Behavior of Biomedical Materials, 87 (2018) 68-79.
[13] Y.S. Jeong, W.J. Kim, Enhancement of mechanical properties and corrosion resistance of Mg–Ca alloys through microstructural refinement by indirect extrusion, Corrosion Science, 82 (2014) 392-403.
[14] Y. Wan, G. Xiong, H. Luo, F. He, Y. Huang, X. Zhou, Preparation and characterization of a new biomedical magnesium–calcium alloy, Materials & Design, 29 (2008) 2034-2037.
[15] Z. Li, X. Gu, S. Lou, Y. Zheng, The development of binary Mg–Ca alloys for use as biodegradable materials within bone, Biomaterials, 29 (2008) 1329-1344.
[16] G.L. Song, A. Atrens, Corrosion Mechanisms of Magnesium Alloys, Advanced Engineering Materials, 1 (1999) 11-33.
[17] N. Erdmann, N. Angrisani, J. Reifenrath, A. Lucas, F. Thorey, D. Bormann, A. Meyer-Lindenberg, Biomechanical testing and degradation analysis of MgCa0.8 alloy screws: A comparative in vivo study in rabbits, Acta Biomaterialia, 7 (2011) 1421-1428.

[18] W.-C. Kim, J.-G. Kim, J.-Y. Lee, H.-K. Seok, Influence of Ca on the corrosion properties of magnesium for biomaterials, Materials Letters, 62 (2008) 4146-4148.
[19] R. Zeng, W. Qi, F. Zhang, H. Cui, Y. Zheng, In vitro corrosion of Mg–1.21Li–1.12Ca–1Y alloy, Progress in Natural Science: Materials International, 24 (2014) 492-499.
[20] M. Mohedano, B.J.C. Luthringer, B. Mingo, F. Feyerabend, R. Arrabal, P.J. Sanchez-Egido, C. Blawert, R. Willumeit-Römer, M.L. Zheludkevich, E. Matykina, Bioactive plasma electrolytic oxidation coatings on Mg-Ca alloy to control degradation behaviour, Surface and Coatings Technology, 315 (2017) 454-467.
[21] N.T. Kirkland, N. Birbilis, J. Walker, T. Woodfield, G.J. Dias, M.P. Staiger, In-vitro dissolution of magnesium–calcium binary alloys: Clarifying the unique role of calcium additions in bioresorbable magnesium implant alloys, Journal of Biomedical Materials Research Part B: Applied Biomaterials, 95B (2010) 91-100.
[22] J.W. Seong, W.J. Kim, Development of biodegradable Mg–Ca alloy sheets with enhanced strength and corrosion properties through the refinement and uniform dispersion of the Mg2Ca phase by high-ratio differential speed rolling, Acta Biomaterialia, 11 (2015) 531-542.
[23] A.D. Südholz, N.T. Kirkland, R.G. Buchheit, N. Birbilis, Electrochemical Properties of Intermetallic Phases and Common Impurity Elements in Magnesium Alloys, Electrochemical and Solid-State Letters, 14 (2011) C5-C7.
[24] E. Zhang, L. Yang, Microstructure, mechanical properties and bio-corrosion properties of Mg–Zn–Mn–Ca alloy for biomedical application, Materials Science and Engineering: A, 497 (2008) 111-118.
[25] M. Deng, D. Höche, S.V. Lamaka, L. Wang, M.L. Zheludkevich, Revealing the impact of second phase morphology on discharge properties of binary Mg-Ca anodes for primary Mg-air batteries, Corrosion Science, 153 (2019) 225-235.
[26] E. Zhang, L. Yang, J. Xu, H. Chen, Microstructure, mechanical properties and bio-corrosion properties of Mg–Si(–Ca, Zn) alloy for biomedical application, Acta Biomaterialia, 6 (2010) 1756-1762.
[27] D.-s. Yin, E.-l. Zhang, S.-y. Zeng, Effect of Zn on mechanical property and corrosion property of extruded Mg-Zn-Mn alloy, Transactions of Nonferrous Metals Society of China, 18 (2008) 763-768.
[28] S. Cai, T. Lei, N. Li, F. Feng, Effects of Zn on microstructure, mechanical properties and corrosion behavior of Mg–Zn alloys, Materials Science and Engineering: C, 32 (2012) 2570-2577.
[29] H. Du, Z. Wei, X. Liu, E. Zhang, Effects of Zn on the microstructure, mechanical property and bio-corrosion property of Mg–3Ca alloys for biomedical application, Materials Chemistry and Physics, 125 (2011) 568-575.
[30] P.-R. Cha, H.-S. Han, G.-F. Yang, Y.-C. Kim, K.-H. Hong, S.-C. Lee, J.-Y. Jung, J.-P. Ahn, Y.-Y. Kim, S.-Y. Cho, J.Y. Byun, K.-S. Lee, S.-J. Yang, H.-K. Seok, Biodegradability engineering of biodegradable Mg alloys: Tailoring the electrochemical properties and microstructure of constituent phases, Scientific Reports, 3 (2013) 2367.
[31] Y. Sun, B. Zhang, Y. Wang, L. Geng, X. Jiao, Preparation and characterization of a new biomedical Mg–Zn–Ca alloy, Materials & Design, 34 (2012) 58-64.
[32] H.R. Bakhsheshi-Rad, M.R. Abdul-Kadir, M.H. Idris, S. Farahany, Relationship between the corrosion behavior and the thermal characteristics and microstructure of Mg–0.5Ca–xZn alloys, Corrosion Science, 64 (2012) 184-197.
[33] P. Doležal, J. Zapletal, S. Fintová, Z. Trojanová, M. Greger, P. Roupcová, T. Podrábský, Influence of Processing Techniques on Microstructure and Mechanical Properties of a Biodegradable Mg-3Zn-2Ca Alloy, Materials, 9 (2016) 880.
[34] Y. Jang, Z. Tan, C. Jurey, Z. Xu, Z. Dong, B. Collins, Y. Yun, J. Sankar, Understanding corrosion behavior of Mg–Zn–Ca alloys from subcutaneous mouse model: Effect of Zn element concentration and plasma electrolytic oxidation, Materials Science and Engineering: C, 48 (2015) 28-40.
[35] G. Song, A. Atrens, M. Dargusch, Influence of microstructure on the corrosion of diecast AZ91D, Corrosion Science, 41 (1998) 249-273.

[36] M. Esmaily, D.B. Blücher, J.E. Svensson, M. Halvarsson, L.G. Johansson, New insights into the corrosion of magnesium alloys — The role of aluminum, Scripta Materialia, 115 (2016) 91-95.
[37] D. Zander, N.A. Zumdick, Influence of Ca and Zn on the microstructure and corrosion of biodegradable Mg–Ca–Zn alloys, Corrosion Science, 93 (2015) 222-233.
[38] S. Gaur, R.K. Singh Raman, A.S. Khanna, In vitro investigation of biodegradable polymeric coating for corrosion resistance of Mg-6Zn-Ca alloy in simulated body fluid, Materials Science and Engineering: C, 42 (2014) 91-101.
[39] L.B. Tong, Q.X. Zhang, Z.H. Jiang, J.B. Zhang, J. Meng, L.R. Cheng, H.J. Zhang, Microstructures, mechanical properties and corrosion resistances of extruded Mg–Zn–Ca–xCe/La alloys, Journal of the Mechanical Behavior of Biomedical Materials, 62 (2016) 57-70.
[40] V. Roche, G.Y. Koga, T.B. Matias, C.S. Kiminami, C. Bolfarini, W.J. Botta, R.P. Nogueira, A.M. Jorge Junior, Degradation of biodegradable implants: The influence of microstructure and composition of Mg-Zn-Ca alloys, Journal of Alloys and Compounds, 774 (2019) 168-181.
[41] D. Mei, S.V. Lamaka, C. Feiler, M.L. Zheludkevich, The effect of small-molecule bio-relevant organic components at low concentration on the corrosion of commercially pure Mg and Mg-0.8Ca alloy: An overall perspective, Corrosion Science, 153 (2019) 258-271.
[42] M. Liu, G.-L. Song, Impurity control and corrosion resistance of magnesium–aluminum alloy, Corrosion Science, 77 (2013) 143-150.
[43] Y. Zhang, J. Li, H. Lai, Y. Xu, Effect of Homogenization on Microstructure Characteristics, Corrosion and Biocompatibility of Mg-Zn-Mn-xCa Alloys, Materials, 11 (2018) 227.
[44] F. Andreatta, I. Apachitei, A.A. Kodentsov, J. Dzwonczyk, J. Duszczyk, Volta potential of second phase particles in extruded AZ80 magnesium alloy, Electrochimica Acta, 51 (2006) 3551-3557.
[45] G. Ben-Hamu, D. Eliezer, K.S. Shin, The role of Si and Ca on new wrought Mg–Zn–Mn based alloy, Materials Science and Engineering: A, 447 (2007) 35-43.
[46] V. Kree, J. Bohlen, D. Letzig, K.U. Kainer, Metallographische Gefügeuntersuchungen von Magnesiumlegierungen, Praktische Metallographie, 41 (2004) 233-246.
[47] H. Abrams, Grain size measurement by the intercept method, Metallography, 4 (1971) 59-78.
[48] Pandat software package for calculating phase diagrams and thermodynamic properties of multi-component alloys, in, CompuTherm LLC, 2017.
[49] S.L. Chen, S. Daniel, F. Zhang, Y.A. Chang, X.Y. Yan, F.Y. Xie, R. Schmid-Fetzer, W.A. Oates, The PANDAT software package and its applications, Calphad, 26 (2002) 175-188.
[50] J. Schindelin, I. Arganda-Carreras, E. Frise, V. Kaynig, M. Longair, T. Pietzsch, S. Preibisch, C. Rueden, S. Saalfeld, B. Schmid, J.-Y. Tinevez, D.J. White, V. Hartenstein, K. Eliceiri, P. Tomancak, A. Cardona, Fiji: an open-source platform for biological-image analysis, Nature Methods, 9 (2012) 676.
[51] W.M. Gan, K. Wu, M.Y. Zheng, X.J. Wang, H. Chang, H.G. Brokmeier, Microstructure and mechanical property of the ECAPed Mg2Si/Mg composite, Materials Science and Engineering: A, 516 (2009) 283-289.
[52] Y. Carbonneau, A. Couture, A. Van Neste, R. Tremblay, On the observation of a new ternary MgSiCa phase in Mg-Si alloys, Metallurgical and Materials Transactions A, 29 (1998) 1759-1763.
[53] B.P. Zhang, Y. Wang, L. Geng, Research on Mg-Zn-Ca Alloy as Degradable Biomaterial, in: R. Pignatello (Ed.) Biomaterials - Physics and Chemistry, IntechOpen, 2011.
[54] K. Kubok, L. Litynska-Dobrzynska, J. Wojewoda-Budka, A. Góral, A. Debski, Investigation of Structures in As-Cast Alloys from the Mg-Zn-Ca System, Archives of Metallurgy and Materials, 58 (2013) 329.
[55] P.M. Jardim, G. Solórzano, J.B.V. Sande, Precipitate Crystal Structure Determination in Melt Spun Mg-1.5wt%Ca-6wt%Zn Alloy, Microscopy and Microanalysis, 8 (2002) 487-496.
[56] A. Kozlov, M. Ohno, R. Arroyave, Z.K. Liu, R. Schmid-Fetzer, Phase equilibria, thermodynamics and solidification microstructures of Mg–Sn–Ca alloys, Part 1: Experimental investigation and thermodynamic modeling of the ternary Mg–Sn–Ca system, Intermetallics, 16 (2008) 299-315.
[57] G. Levi, S. Avraham, A. Zilberov, M. Bamberger, Solidification, solution treatment and age hardening of a Mg–1.6wt.% Ca–3.2wt.% Zn alloy, Acta Materialia, 54 (2006) 523-530.

[58] K. Oh-ishi, R. Watanabe, C.L. Mendis, K. Hono, Age-hardening response of Mg–0.3at.%Ca alloys with different Zn contents, Materials Science and Engineering: A, 526 (2009) 177-184.
[59] S.W. Xu, K. Oh-ishi, H. Sunohara, S. Kamado, Extruded Mg–Zn–Ca–Mn alloys with low yield anisotropy, Materials Science and Engineering: A, 558 (2012) 356-365.
[60] M. Bornapour, M. Celikin, M. Cerruti, M. Pekguleryuz, Magnesium implant alloy with low levels of strontium and calcium: The third element effect and phase selection improve bio-corrosion resistance and mechanical performance, Materials Science and Engineering: C, 35 (2014) 267-282.
[61] Y. Ai, C.P. Luo, J. Liu, Twinning of CaMgSi phase in a cast Mg–1.0Ca–0.5Si–0.3Zr alloy, Acta Materialia, 55 (2007) 531-538.
[62] T. Hosono, M. Kuramoto, Y. Matsuzawa, Y. Momose, Y. Maeda, T. Matsuyama, H. Tatsuoka, Y. Fukuda, S. Hashimoto, H. Kuwabara, Formation of CaMgSi at Ca2Si/Mg2Si interface, Applied Surface Science, 216 (2003) 620-624.
[63] D. Liu, C. Guo, L. Chai, V.R. Sherman, X. Qin, Y. Ding, M.A. Meyers, Mechanical properties and corrosion resistance of hot extruded Mg–2.5Zn–1Ca alloy, Materials Science and Engineering: B, 195 (2015) 50-58.
[64] Y. Lu, A.R. Bradshaw, Y.L. Chiu, I.P. Jones, Effects of secondary phase and grain size on the corrosion of biodegradable Mg–Zn–Ca alloys, Materials Science and Engineering: C, 48 (2015) 480-486.
[65] Z. Xu, C. Smith, S. Chen, J. Sankar, Development and microstructural characterizations of Mg–Zn–Ca alloys for biomedical applications, Materials Science and Engineering: B, 176 (2011) 1660-1665.
[66] J. Hofstetter, S. Rüedi, I. Baumgartner, H. Kilian, B. Mingler, E. Povoden-Karadeniz, S. Pogatscher, P.J. Uggowitzer, J.F. Löffler, Processing and microstructure–property relations of high-strength low-alloy (HSLA) Mg–Zn–Ca alloys, Acta Materialia, 98 (2015) 423-432.
[67] M. Yang, T. Guo, H. Li, Effects of Gd addition on as-cast microstructure, tensile and creep properties of Mg–3.8 Zn–2.2Ca (wt%) magnesium alloy, Materials Science and Engineering: A, 587 (2013) 132-142.
[68] J.-W. Chang, P.-H. Fu, X.-W. Guo, L.-M. Peng, W.-J. Ding, The effects of heat treatment and zirconium on the corrosion behaviour of Mg–3Nd–0.2Zn–0.4Zr (wt.%) alloy, Corrosion Science, 49 (2007) 2612-2627.
[69] P. Jiang, C. Blawert, R. Hou, N. Scharnagl, J. Bohlen, M.L. Zheludkevich, Microstructural influence on corrosion behavior of MgZnGe alloy in NaCl solution, Journal of Alloys and Compounds, 783 (2019) 179-192.
[70] D. Battocchi, A.M. Simões, D.E. Tallman, G.P. Bierwagen, Comparison of testing solutions on the protection of Al-alloys using a Mg-rich primer, Corrosion Science, 48 (2006) 2226-2240.
[71] N.C. Verissimo, E.S. Freitas, N. Cheung, A. Garcia, W.R. Osório, The effects of Zn segregation and microstructure length scale on the corrosion behavior of a directionally solidified Mg-25 wt.%Zn alloy, Journal of Alloys and Compounds, 723 (2017) 649-660.
[72] Y. Xin, K. Huo, H. Tao, G. Tang, P.K. Chu, Influence of aggressive ions on the degradation behavior of biomedical magnesium alloy in physiological environment, Acta Biomaterialia, 4 (2008) 2008-2015.
[73] D. Mei, S.V. Lamaka, J. Gonzalez, F. Feyerabend, R. Willumeit-Römer, M.L. Zheludkevich, The role of individual components of simulated body fluid on the corrosion behavior of commercially pure Mg, Corrosion Science, 147 (2019) 81-93.
[74] N.T. Kirkland, N. Birbilis, M.P. Staiger, Assessing the corrosion of biodegradable magnesium implants: A critical review of current methodologies and their limitations, Acta Biomaterialia, 8 (2012) 925-936.
[75] K.S. Novoselov, A.K. Geim, S.V. Morozov, D. Jiang, Y. Zhang, S.V. Dubonos, I.V. Grigorieva, A.A. Firsov, Electric Field Effect in Atomically Thin Carbon Films, Science, 306 (2004) 666-669.
[76] A. Atrens, G.-L. Song, M. Liu, Z. Shi, F. Cao, M.S. Dargusch, Review of Recent Developments in the Field of Magnesium Corrosion, Advanced Engineering Materials, 17 (2015) 400-453.

[77] S. Pawar, T.J.A. Slater, T.L. Burnett, X. Zhou, G.M. Scamans, Z. Fan, G.E. Thompson, P.J. Withers, Crystallographic effects on the corrosion of twin roll cast AZ31 Mg alloy sheet, Acta Materialia, 133 (2017) 90-99.
[78] M. Liu, P. Schmutz, P.J. Uggowitzer, G. Song, A. Atrens, The influence of yttrium (Y) on the corrosion of Mg–Y binary alloys, Corrosion Science, 52 (2010) 3687-3701.
[79] N.I. Zainal Abidin, D. Martin, A. Atrens, Corrosion of high purity Mg, AZ91, ZE41 and Mg2Zn0.2Mn in Hank's solution at room temperature, Corrosion Science, 53 (2011) 862-872.
[80] Y. Xin, T. Hu, P.K. Chu, In vitro studies of biomedical magnesium alloys in a simulated physiological environment: A review, Acta Biomaterialia, 7 (2011) 1452-1459.
[81] T. Kokubo, H. Takadama, How useful is SBF in predicting in vivo bone bioactivity?, Biomaterials, 27 (2006) 2907-2915.
[82] M. Bohner, J. Lemaitre, Can bioactivity be tested in vitro with SBF solution?, Biomaterials, 30 (2009) 2175-2179.
[83] R.-C. Zeng, L. Sun, Y.-F. Zheng, H.-Z. Cui, E.-H. Han, Corrosion and characterisation of dual phase Mg–Li–Ca alloy in Hank's solution: The influence of microstructural features, Corrosion Science, 79 (2014) 69-82.
[84] Y. Xin, T. Hu, P.K. Chu, Influence of Test Solutions on In Vitro Studies of Biomedical Magnesium Alloys, Journal of The Electrochemical Society, 157 (2010) C238-C243.
[85] Y. Chen, G. Wan, J. Wang, S. Zhao, Y. Zhao, N. Huang, Covalent immobilization of phytic acid on Mg by alkaline pre-treatment: Corrosion and degradation behavior in phosphate buffered saline, Corrosion Science, 75 (2013) 280-286.
[86] Y. Zhang, P. Gore, W. Rong, Y. Wu, Y. Yan, R. Zhang, L. Peng, J.-F. Nie, N. Birbilis, Quasi-in-situ STEM-EDS insight into the role of Ag in the corrosion behaviour of Mg-Gd-Zr alloys, Corrosion Science, 136 (2018) 106-118.
[87] H. Matsubara, Y. Ichige, K. Fujita, H. Nishiyama, K. Hodouchi, Effect of impurity Fe on corrosion behavior of AM50 and AM60 magnesium alloys, Corrosion Science, 66 (2013) 203-210.
[88] C. Lin, X. Li, Role of CO2 in the initial stage of atmospheric corrosion of AZ91 magnesium alloy in the presence of NaCl, Rare Metals, 25 (2006) 190-196.
[89] M. Jönsson, D. Persson, D. Thierry, Corrosion product formation during NaCl induced atmospheric corrosion of magnesium alloy AZ91D, Corrosion Science, 49 (2007) 1540-1558.
[90] J. Liu, Y. Song, J. Chen, P. Chen, D. Shan, E.-H. Han, The Special Role of Anodic Second Phases in the Micro-galvanic Corrosion of EW75 Mg Alloy, Electrochimica Acta, 189 (2016) 190-195.
[91] L. Yang, G. Liu, L. Ma, E. Zhang, X. Zhou, G. Thompson, Effect of iron content on the corrosion of pure magnesium: Critical factor for iron tolerance limit, Corrosion Science, 139 (2018) 421-429.
[92] L. Yang, X. Zhou, S.-M. Liang, R. Schmid-Fetzer, Z. Fan, G. Scamans, J. Robson, G. Thompson, Effect of traces of silicon on the formation of Fe-rich particles in pure magnesium and the corrosion susceptibility of magnesium, Journal of Alloys and Compounds, 619 (2015) 396-400.
[93] C. Zhao, F. Pan, S. Zhao, H. Pan, K. Song, A. Tang, Preparation and characterization of as-extruded Mg–Sn alloys for orthopedic applications, Materials & Design, 70 (2015) 60-67.

Table 1. Chemical composition of Mg-0.5Zn-0.2Ca alloy determined by ICP-OES

Composition (wt. %)				
Zn	Ca	Mn	Si	Al
0.52 ± 0.02	0.20 ± 0.02	0.0193 ± 0.0005	0.0145 ± 0.0004	0.0043 ± 0.0005
Fe	Cu	Ni	Be	Mg
0.0021 ± 0.0006	< 0.0003	< 0.0003	< 0.0003	Bal.

Table 2. SEM EDS results of the IMPs in the as-cast and the solution-annealed Mg-0.5Zn-0.2Ca alloy

	as-cast			solution-annealed
particles	Mg-Ca-Si-containing	Mg-Zn-Ca-containing	Mg-Ca-containing	Mg-Ca-Si-containing
O at.%	1.87 ± 0.97	1.75 ± 0.52	3.17 ± 4.59	1.28 ± 1.10
Mg at.%	86.27 ± 6.64	81.33 ± 5.42	82.70 ± 5.36	87.34 ± 4.70
Si at.%	6.44 ± 3.51	0.16 ± 0.07	0.14 ± 0.12	6.09 ± 1.98
Ca at.%	5.06 ± 2.64	6.61 ± 2.22	10.88 ± 4.87	4.79 ± 1.68
Zn at.%	0.36 ± 0.15	10.15 ± 3.39	2.94 ± 0.98	0.48 ± 0.25
Zn/Ca	-	1.59 ± 0.41	-	-
Ca/Si	0.81 ± 0.09	-	-	0.79 ± 0.13

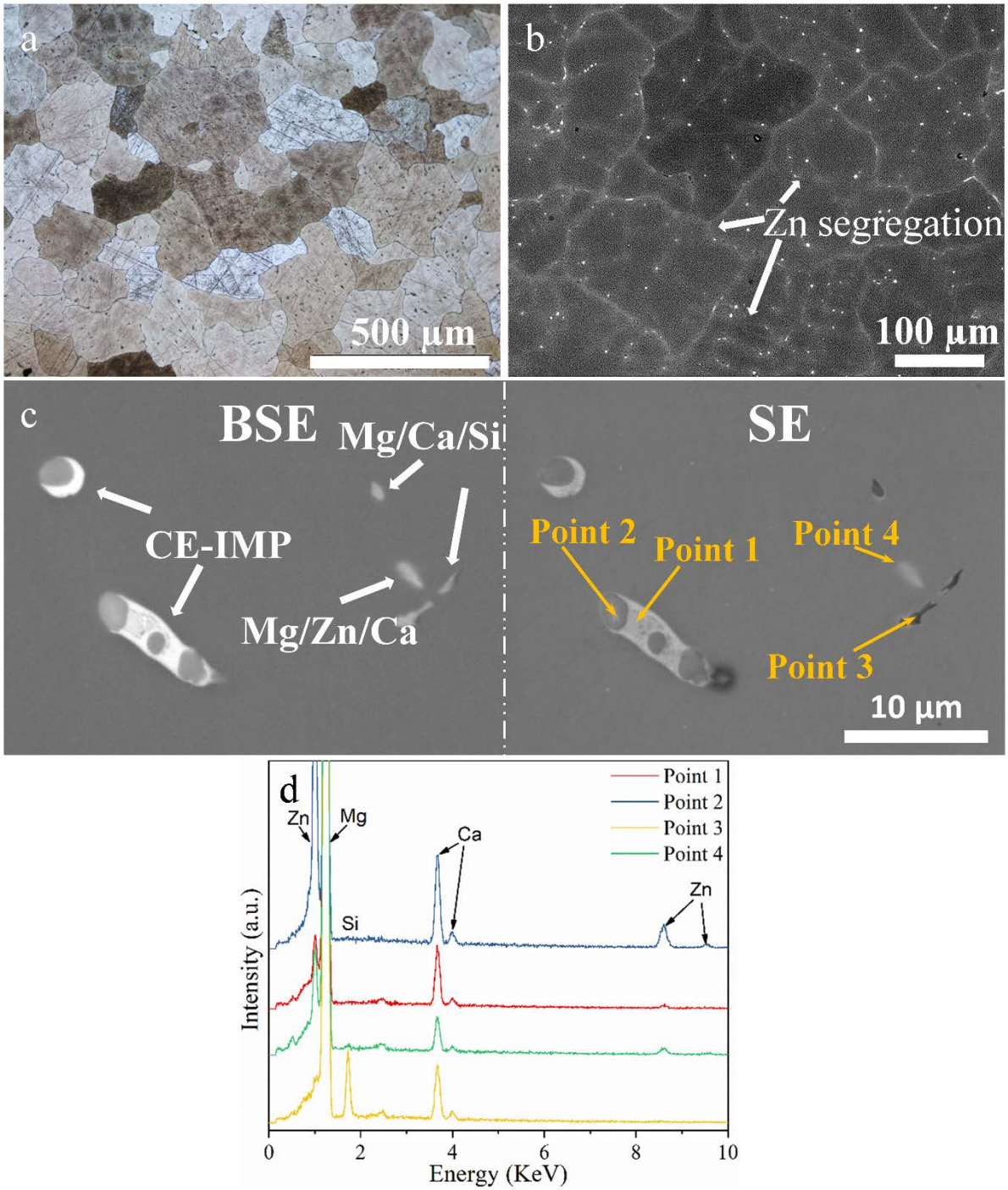

Fig. 1. Microstructure of the as-cast Mg-0.5Zn-0.2Ca alloy indicated by (a) OM image and (b) SEM image in BSE mode; intermetallic phases indicated by (c) SEM images in BSE and SE mode: isolated Mg/Zn/Ca-containing phase, Mg/Ca/Si-containing phase and co-existing intermetallic particle (CE-IMP); (d) SEM EDS spectra conducted on point 1-4

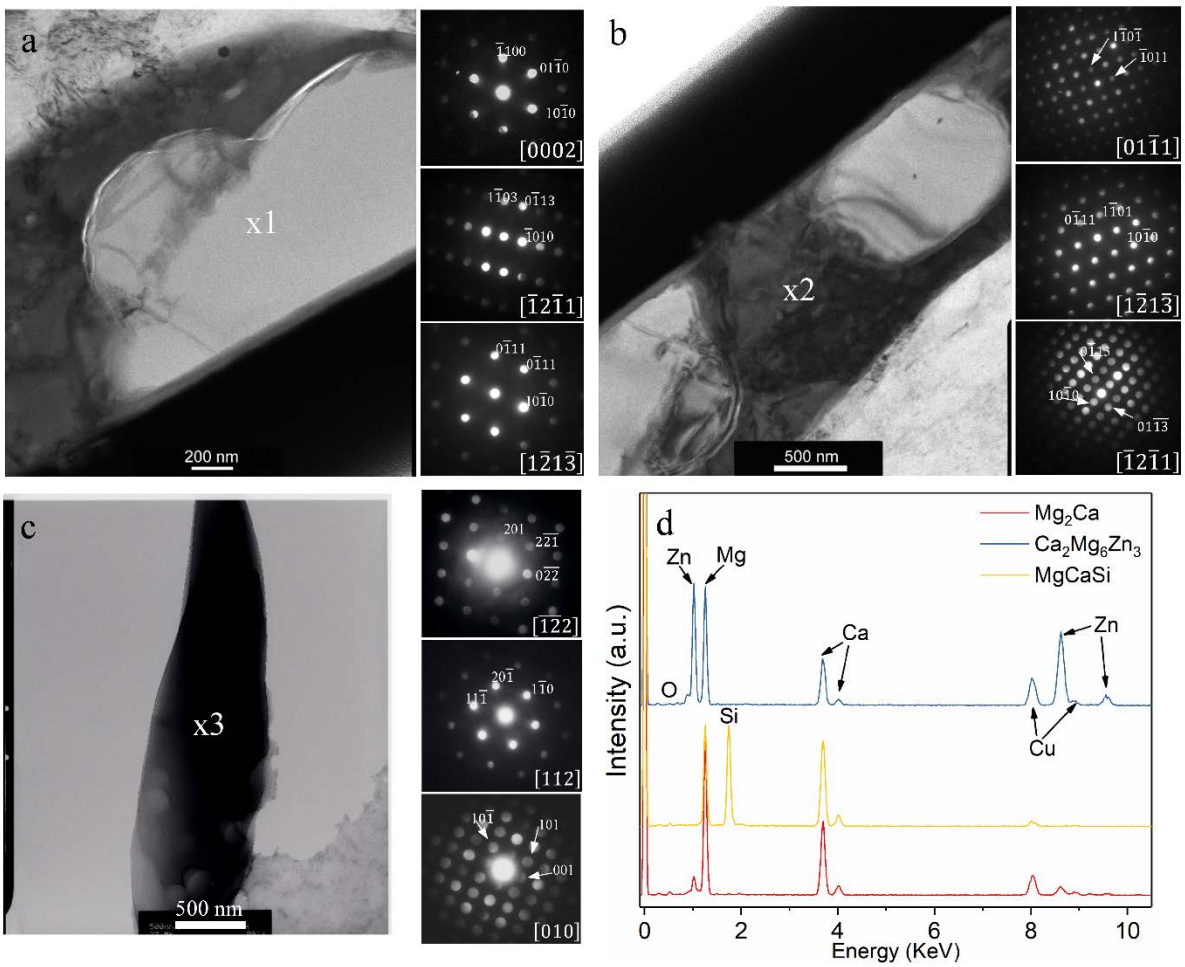

Fig. 2. TEM SAED patterns of (a) Mg_2Ca, (b) $Ca_2Mg_6Zn_3$ in CE-IMP and (c) MgCaSi phase in the as-cast Mg-0.5Zn-0.2Ca alloy; (d) TEM EDS spectra of spot x1, x2, x3 in (a-c)

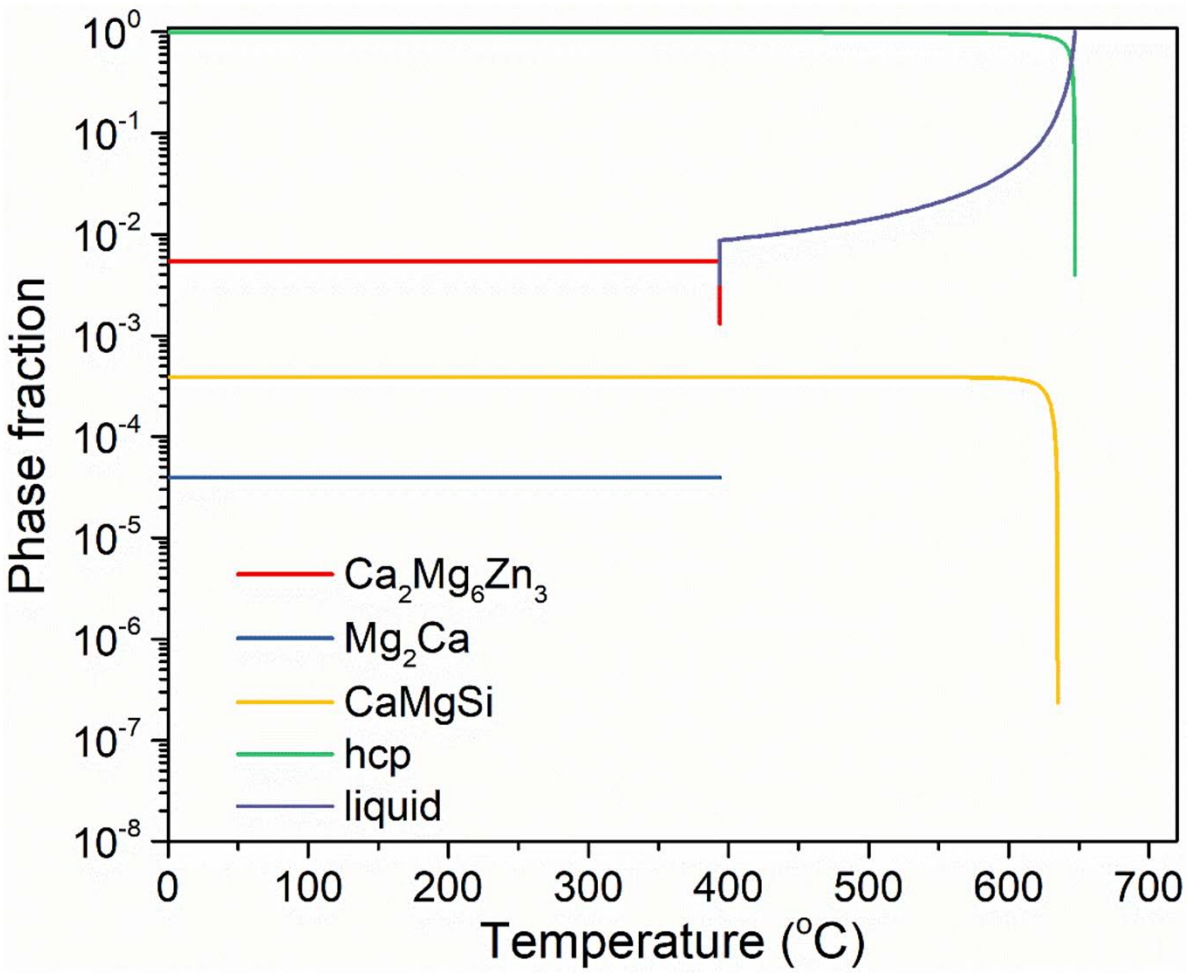

Fig. 3. Phase fraction of IMPs, hcp Mg and liquid of the as-cast Mg-0.5Zn-0.2Ca alloy in dependence of temperature using a Scheil model by Pandat^{TM}2017 with PanMagnesium 2017 database

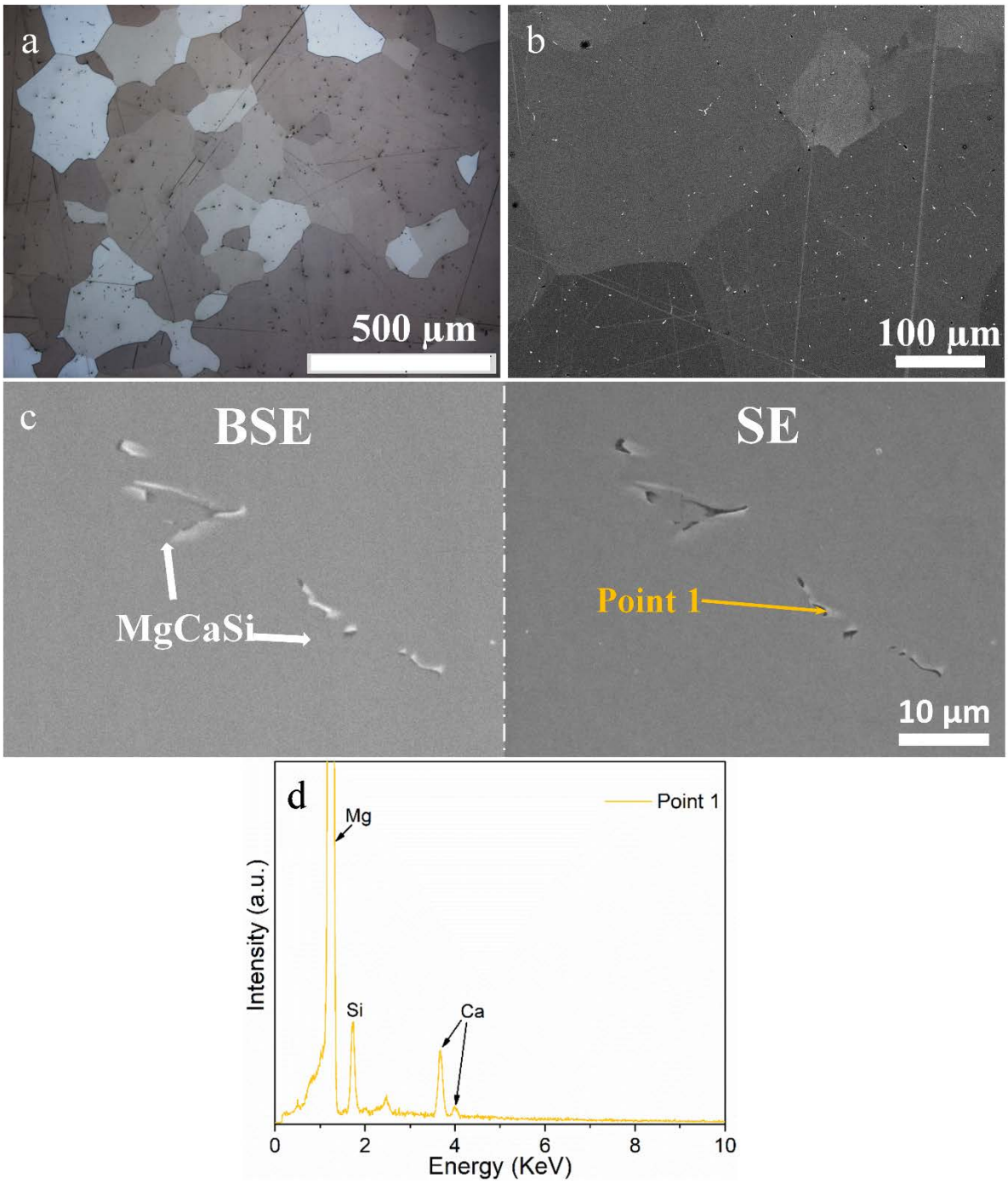

Fig. 4. Microstructure of the solution-annealed Mg-0.5Zn-0.2Ca alloy indicated by (a) OM image and (b) SEM image in BSE mode; intermetallic phase indicated by (c) SEM images in BSE and SE mode: Mg/Ca/Si-containing phase; (d) SEM EDS spectrum conducted on point 1

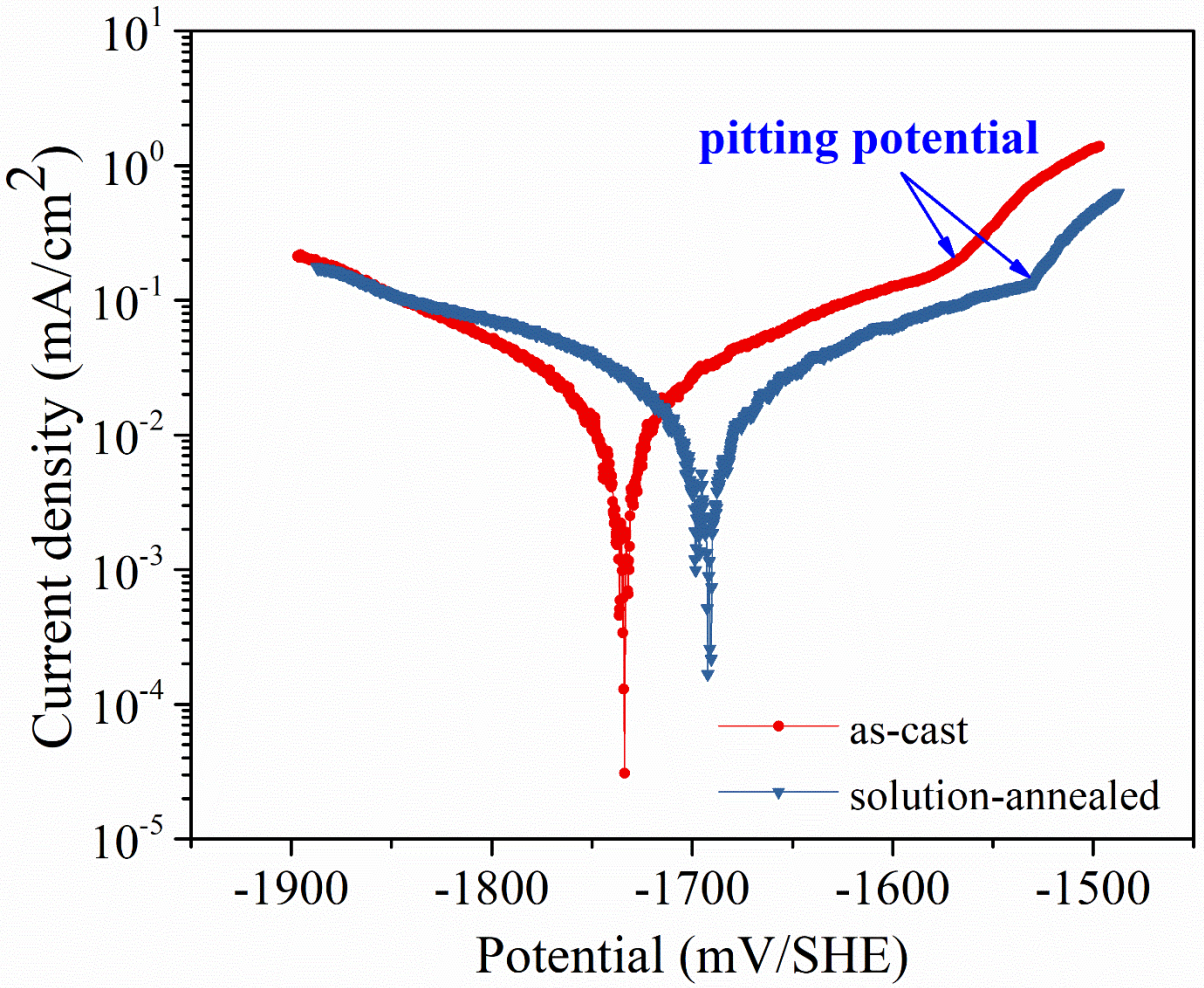

Fig. 5. PDP of the as-cast and solution-annealed Mg-0.5Zn-0.2Ca alloy

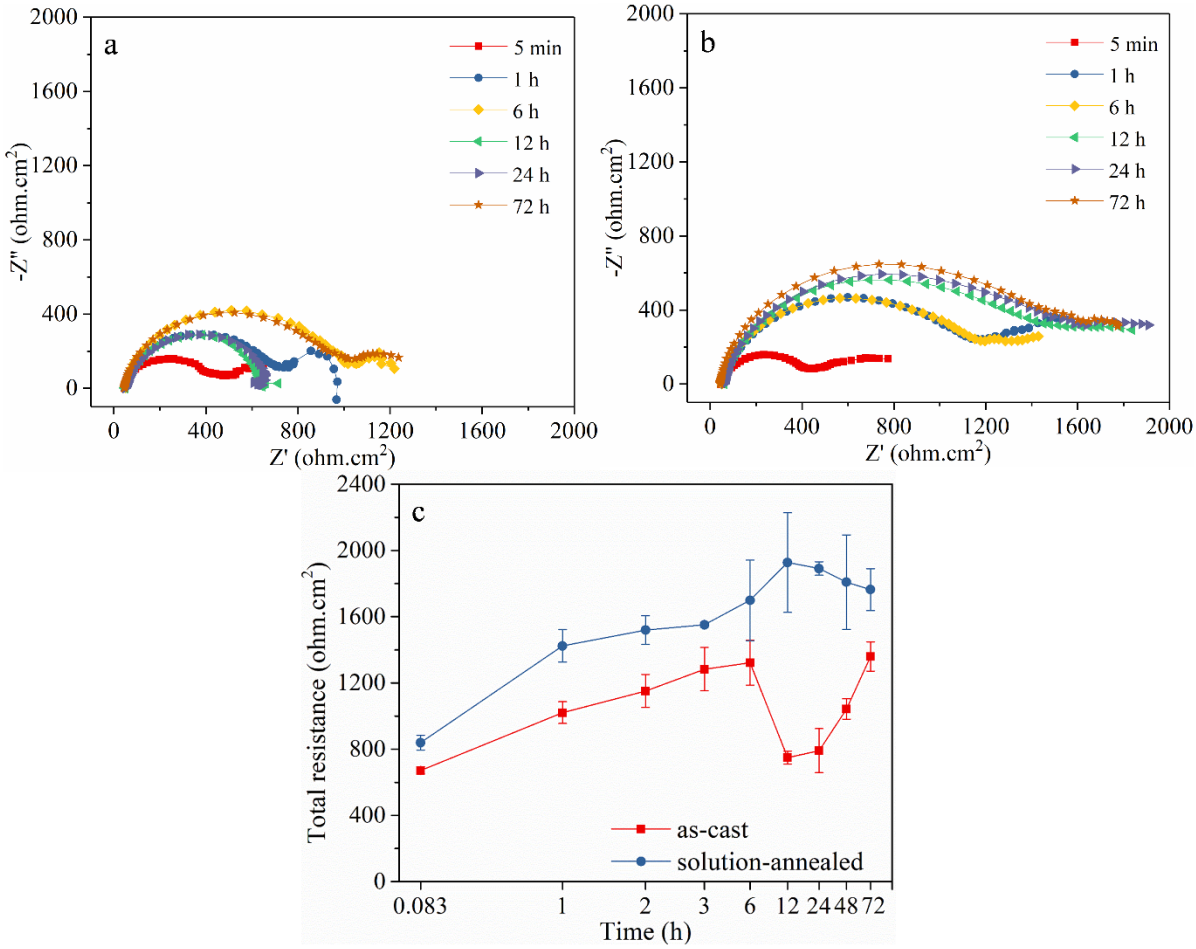

Fig. 6. Nyquist plots of the (a) as-cast and (b) solution annealed Mg-0.5Zn-0.2Ca alloy; (c) variation of total resistance value at 0.1 Hz during 3 days measurement (the X axis is in log10 scale for better perception)

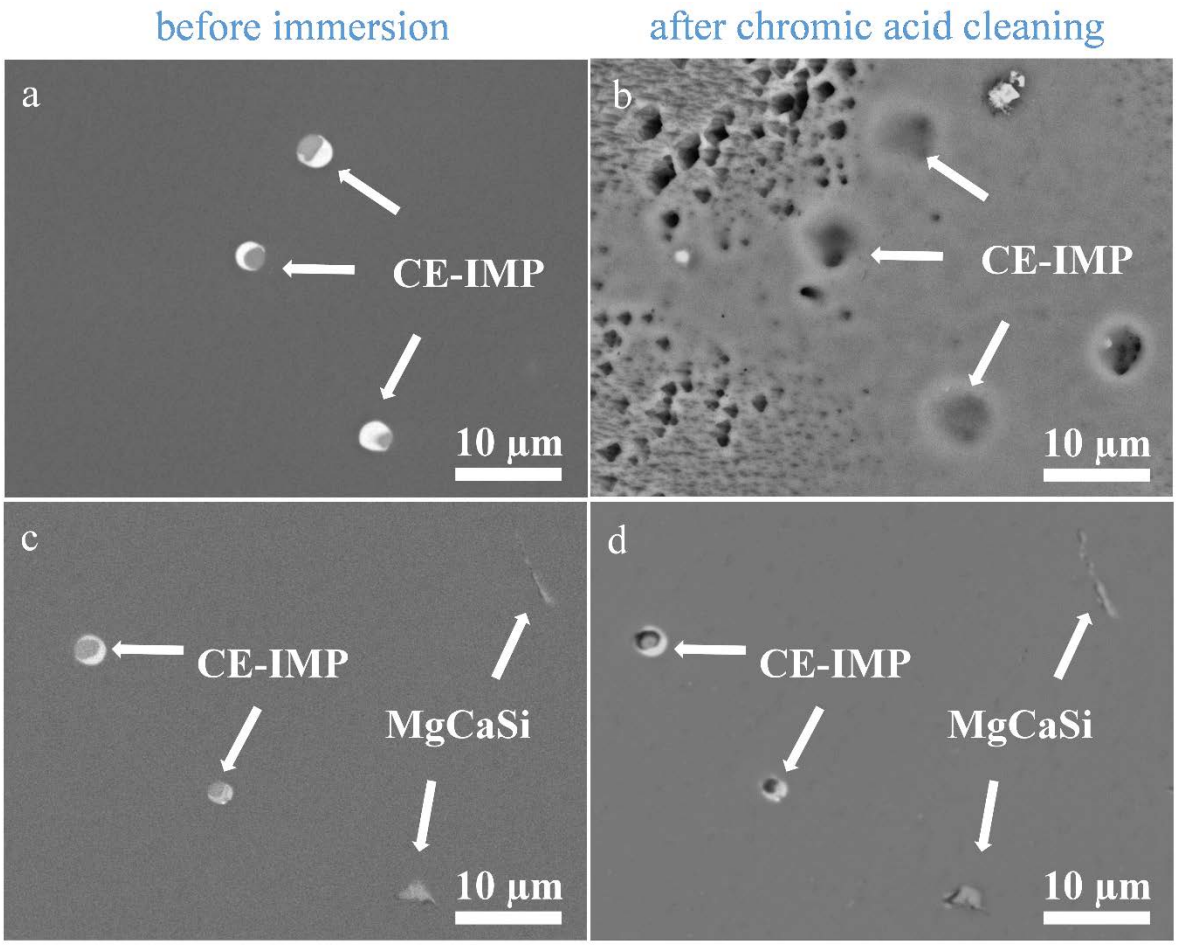

Fig. 7. SEM images in BSE mode of as-cast Mg-0.5Zn-0.2Ca alloy (a) before and (b) after fresh chromic acid cleaning; (c) before and (d) after diluted chromic acid cleaning

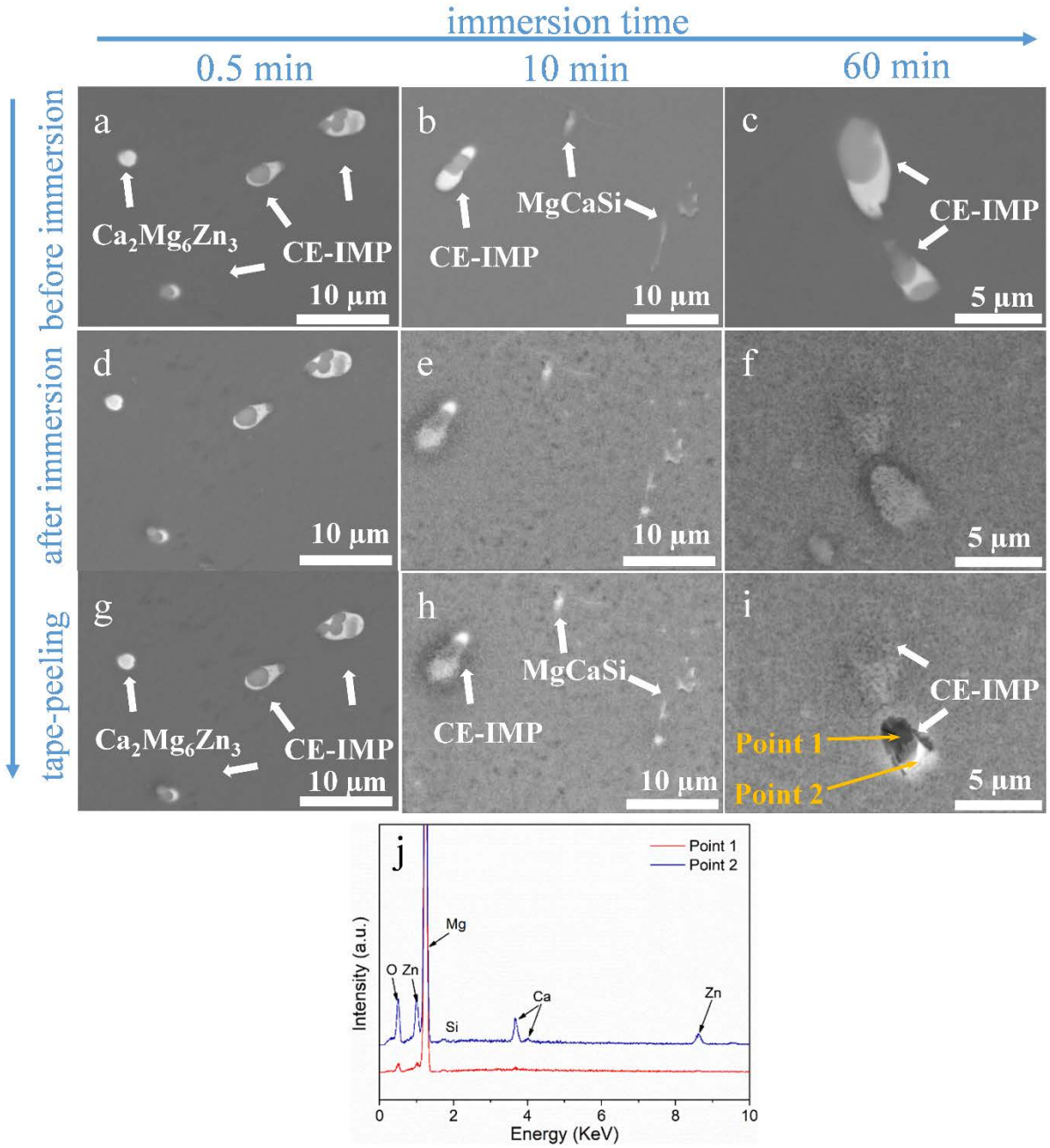

Fig. 8. SEM images in BSE mode of the as-cast Mg-0.5Zn-0.2Ca alloy (a-c) before immersion, (d-f) after immersion for 0.5 min, 10 min and 60 min, respectively; (g-i) after tape-peeling process to remove the corrosion products; (j) SEM EDS spectra of point 1 and 2

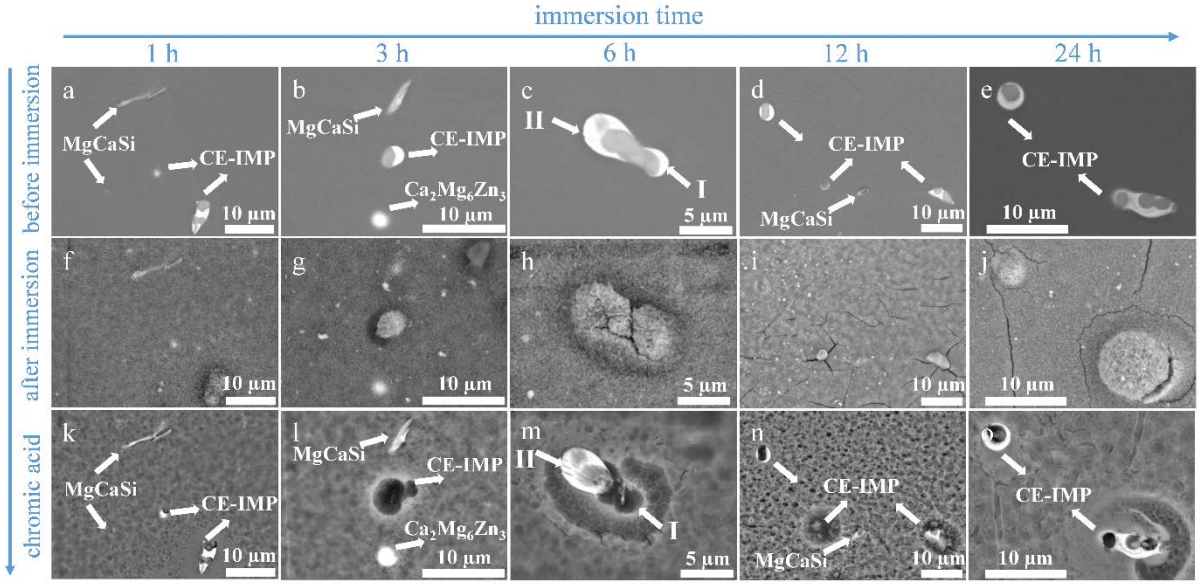

Fig. 9. SEM images in BSE mode of as-cast Mg-0.5Zn-0.2Ca alloy (a-e) before immersion; after immersion for (f) 1 h, (g) 3 h, (h) 6 h, (i) 12 h and (j) 24 h, respectively; (k-o) after diluted chromic acid to remove the corrosion products

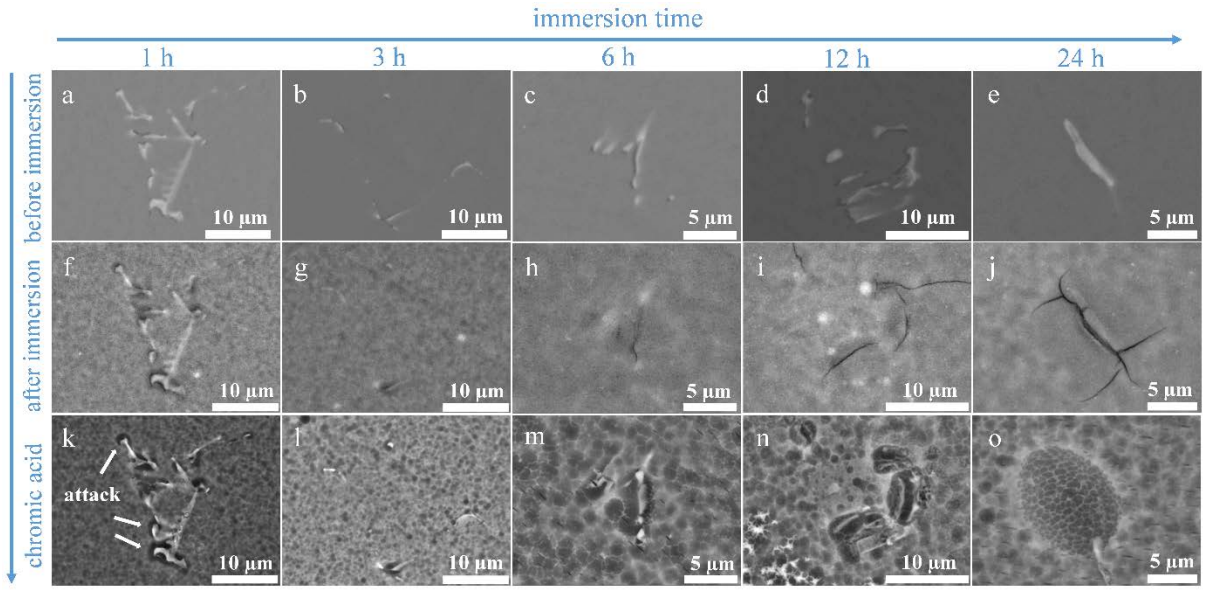

Fig. 10. SEM images in BSE mode of solution-annealed Mg-0.5Zn-0.2Ca alloy (a-e) before immersion; after immersion for (f) 1 h, (g) 3 h, (h) 6 h, (i) 12 h and (j) 24 h, respectively; (k-o) after diluted chromic acid to remove the corrosion products

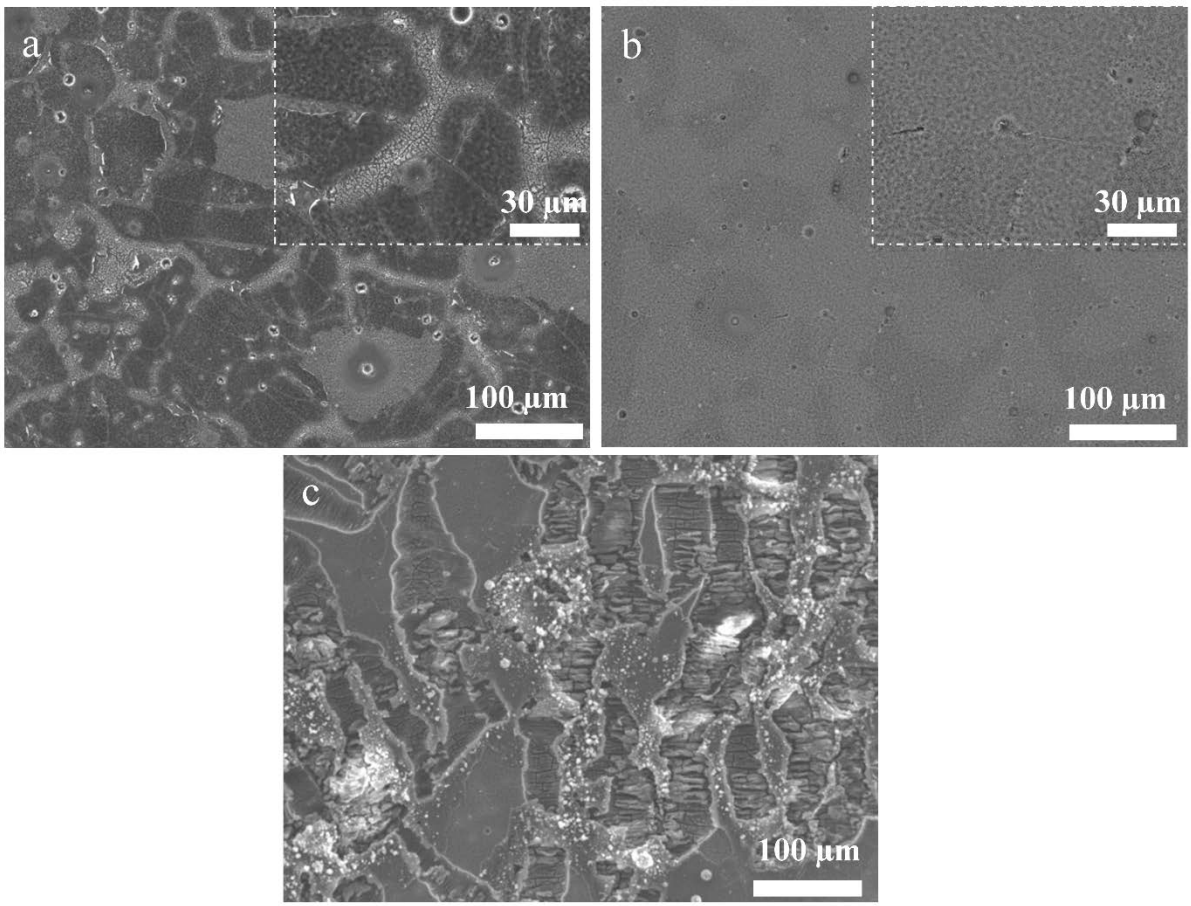

Fig. 11. SEM images in BSE mode of (a) as-cast and (b) solution-annealed Mg-0.5Zn-0.2Ca alloy after immersion for 24 h; (c) selective corrosion morphology of as-cast Mg-0.5Zn-0.2Ca alloy after immersion for 6 h

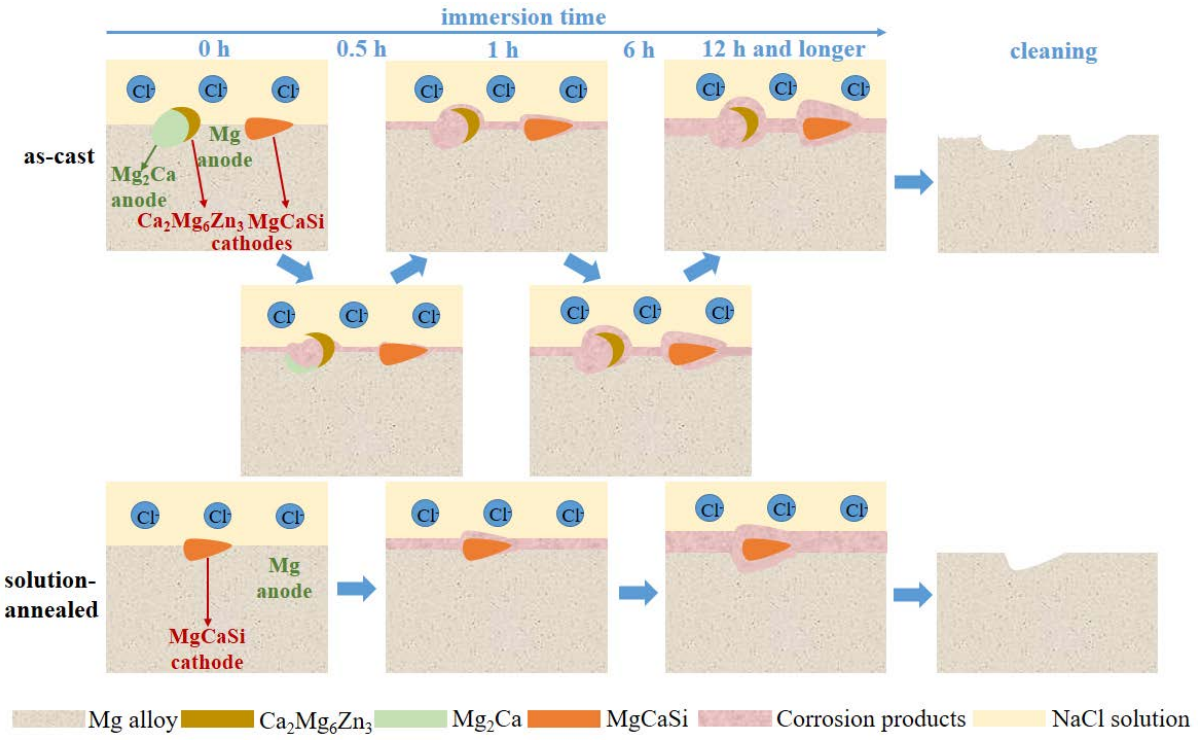

Fig. 12. Sketch of the corrosion behaviour of the as-cast and solution-annealed Mg-0.5Zn-0.2Ca alloy during immersion

Supporting information

Time-sequential corrosion behaviour observation of micro-alloyed Mg-0.5Zn-0.2Ca alloy via a quasi-in situ approach

Yiming Jin[1]*, Carsten Blawert[2], Frank Feyerabend[1], Jan Bohlen[2], Maria Silva Campos[2], Sarkis Gavras[2], Björn Wiese[1], Di Mei[2], Min Deng[2], Hong Yang[2], Regine Willumeit-Römer[1,3]

1 Institute of Metallic Biomaterials, Helmholtz-Zentrum Geesthacht, 21502 Geesthacht, Germany

2 Magnesium Innovation Center, Helmholtz-Zentrum Geesthacht, 21502 Geesthacht, Germany

3 Faculty of Engineering, Christian-Albrechts-Universität zu Kiel, 24143 Kiel, Germany

*E-mail: yiming.jin@hzg.de

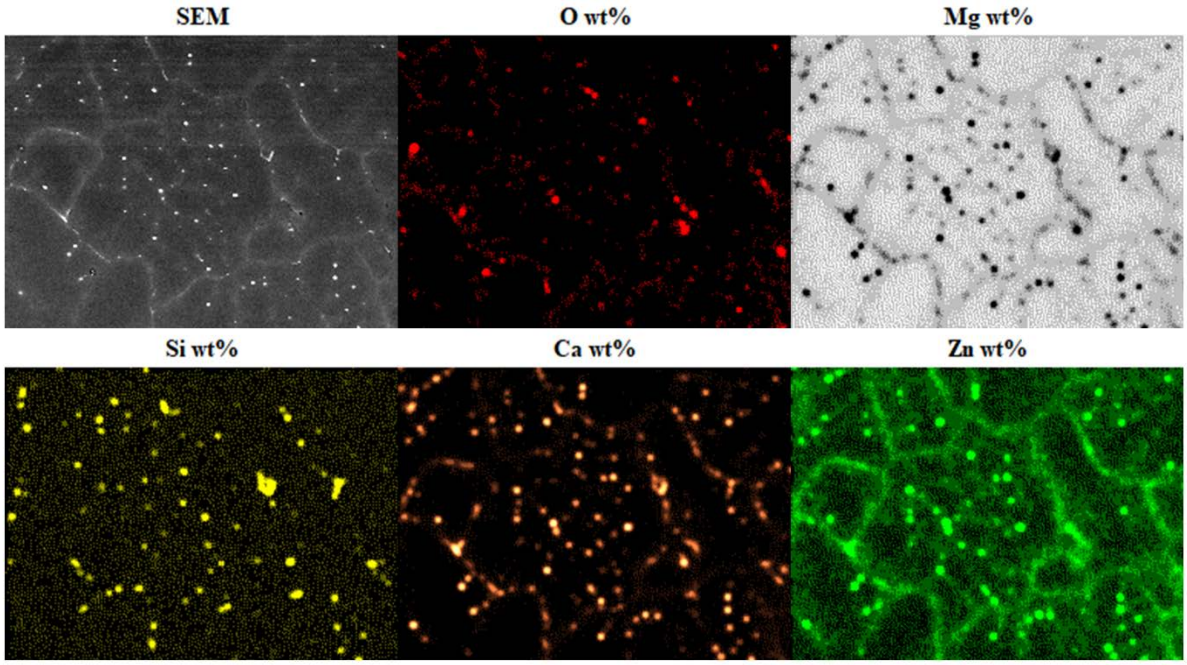

Fig. S1 EDS element mapping of the as-cast Mg-0.5Zn-0.2Ca alloy

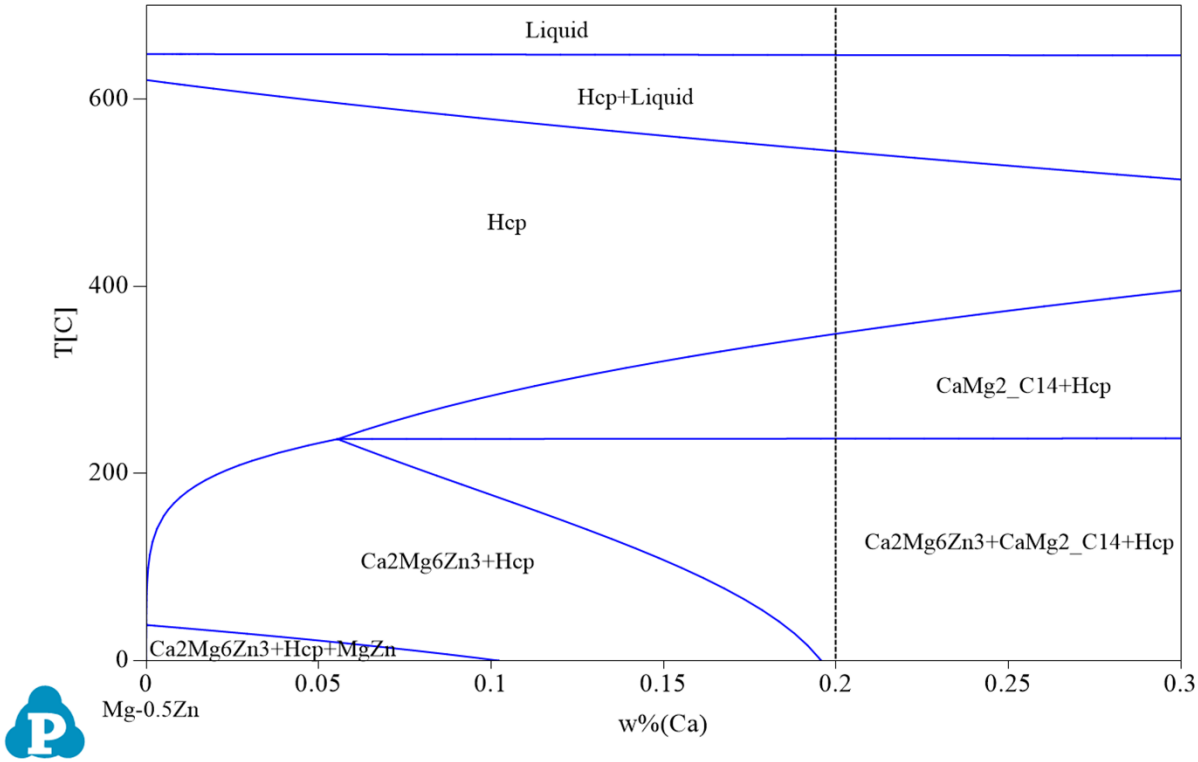

Fig. S2 Thermodynamic calculated phase diagram of Mg-0.5Zn-Ca system by Pandat^{TM} 2017 with PanMagnesium 2017 database

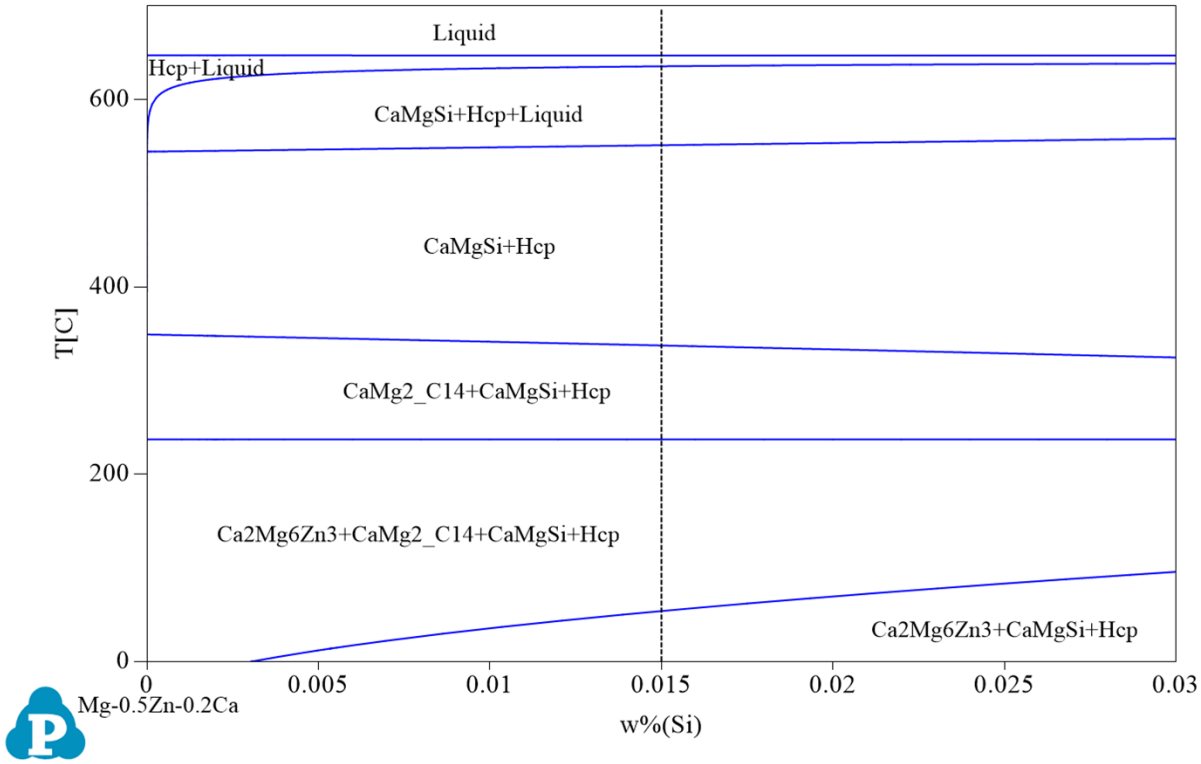

Fig. S3 Thermodynamic calculated phase diagram of Mg-0.5Zn-0.2Ca-Si system by Pandat^{TM} 2017 with PanMagnesium 2017 database

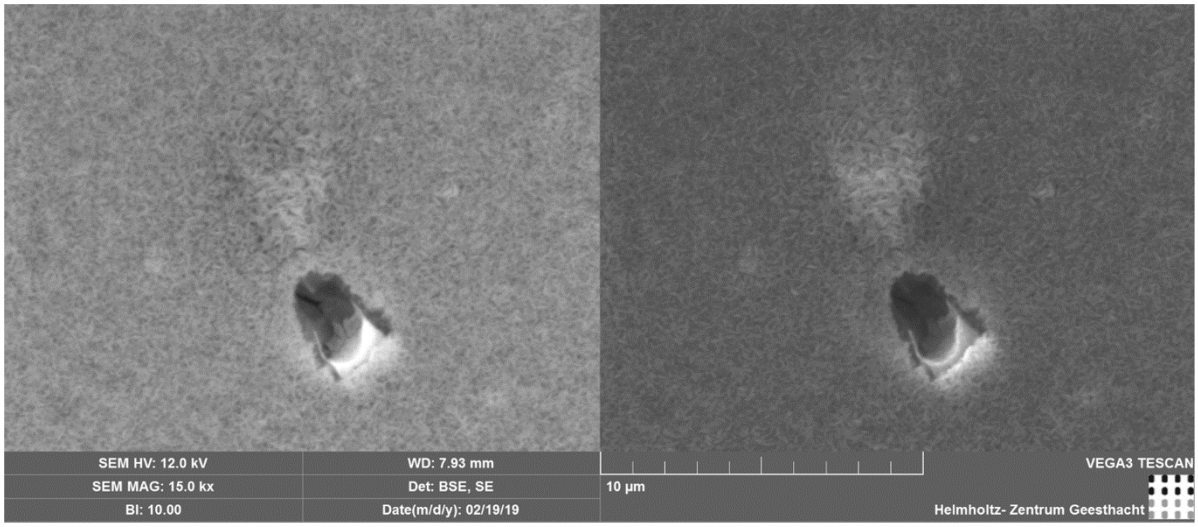

Fig. S4 SEM image in BSE and SE mode of the same location corresponding to Fig. 8

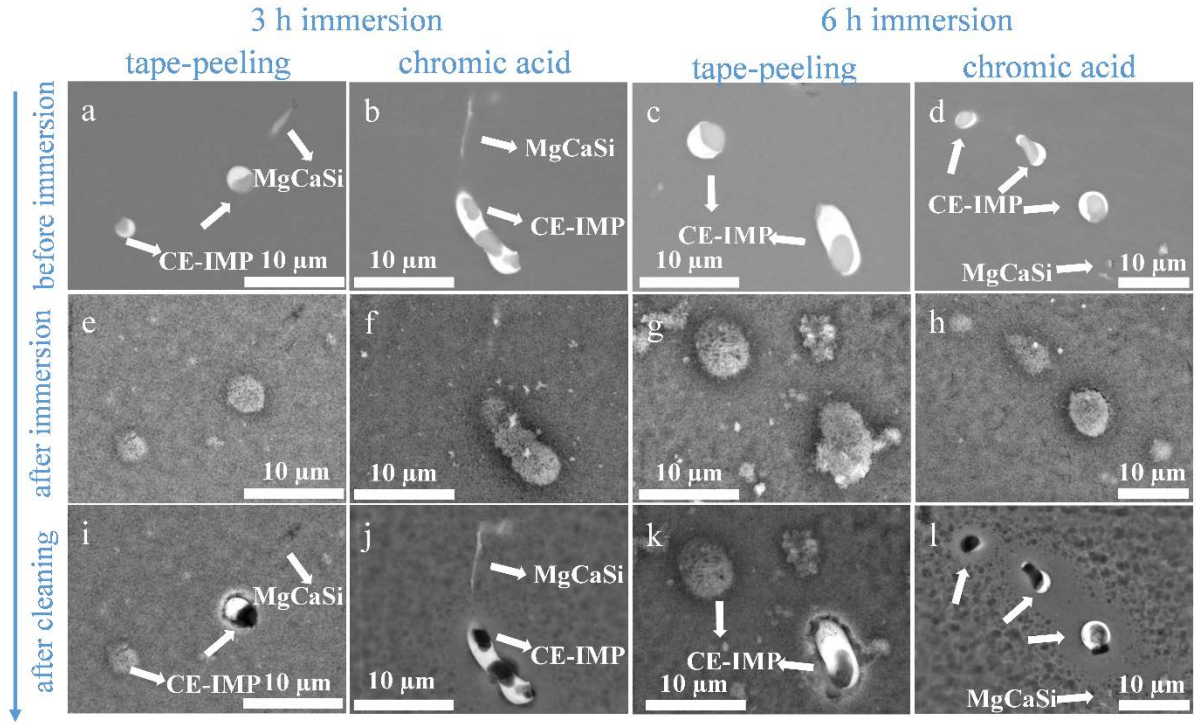

Fig. S5. SEM images in BSE mode of the as-cast Mg-0.5Zn-0.2Ca alloy (a)(b)(c)(d) before immersion; after immersion for (e)(f) 3 h and (g)(h) 6 h, respectively; after (i)(k) tape-peeling process and (j)(l) diluted chromic acid to remove the corrosion products